Modeling and LES of High-Pressure Liquid Injection Under Evaporating and Non-Evaporating Conditions by a Real Fluid Model and Surface Density Approach

Hesham Gaballa, Chaouki Habchi, Jean-Charles de Hemptinne

Modeling and LES of high-pressure liquid injection under evaporating and non-evaporating conditions by a real fluid model and surface density approach

Hesham Gaballa*, Chaouki Habchi*, Jean-Charles de Hemptinne

IFP Energies Nouvelles, Institut Carnot Transports Energies, 1 et 4 Avenue de Bois-Préau, 92852 Rueil-Malmaison, France

Abstract

Numerical modeling of high-pressure liquid fuel injection remains a challenge in various applications. Indeed, experimental observations have shown that injected liquid fuel jet undergoes a continuous change of state from classical two-phase atomization and spray droplets evaporation to a dense-fluid mixing phenomenon depending on the ambient pressure, temperature, and fuel properties. Accordingly, a predictive and efficient computational fluid dynamics (CFD) model that can represent the possible coexistence of subcritical and supercritical regimes during the fuel injection event is required The widely used Lagrangian Discrete Droplet Method (DDM) requires parameter tuning of model constants and cannot model the dense near-nozzle region. Meanwhile, the high computational cost of Interface Capturing Methods (ICM) has prohibited their application to industrial cases. Thus, another alternative is an Eulerian Diffuse Interface Model (DIM), where the unresolved interface features are modeled instead of being tracked. Accordingly, the current work proposes a fully compressible multi-component two-phase real-fluid model (RFM) with a diffused interface and closed by a thermodynamic equilibrium tabulation method based on a real-fluid equation of state. The RFM model is complemented with a postulated surface density equation for fuel atomization modeling within the Large Eddy Simulation (LES) framework. The Engine Combustion Network (ECN) Spray A injector non-evaporating and nominal evaporating conditions are used as a reference for the proposed model validation. Simulations are performed using the proposed RFM model that has been implemented in the CONVERGE CFD solver. Under the non-evaporating condition, the RFM model can capture well the fuel mass distribution in the near-nozzle field, but also the interfacial surface area. Besides, the predicted drop size from simulations falls within the experimental data range. On the other hand, under the evaporating condition, spray liquid and vapor penetrations and fuel mixture fraction distribution are also accurately predicted. The vaporization effect on the surface area density is revealed to enhance surface generation in the dense spray region while reducing the surface density in the dilute spray region. The mean droplet size is also

*Corresponding author, Email: chawki.habchi@ifpen.fr (C.H.); hesham.gaballa@ifpen.fr (H.G.)

Preprint submitted to International Journal of Multi-phase flow, 20 December 2022

relatively reduced under the evaporating condition in the diluted spray region. Overall, the accuracy and computationally efficiency of the proposed RFM model coupled with the surface density equation for high-pressure fuel injection modeling are confirmed, allowing its use for high pressure industrial configurations in future studies.

Keywords: Real-fluid model; Thermodynamic tabulation; Vapor-liquid equilibrium; Large eddy simulation; Atomization; Engine Combustion Network (ECN) Spray A;

1 Introduction

Fuel injection is an essential step toward the combustion process in various applications, including internal combustion engines, gas turbines, and rocket engines. Indeed, the preparation of the fuel-ambient gases mixture significantly affects the combustion efficiency and emissions formation. Computational fluid dynamics (CFD) models capable of simulating fuel injection under various operating conditions are thus essential for the design and optimization of fuel injection equipment (FIE). However, modeling of fuel injection and combustion remains a challenge due to the variety of length and time scales and the involved physical processes during the injection process [67, 10, 22, 41, 62]. The physical processes include in-nozzle cavitation, liquid atomization, phase-change, mixing, and chemical reactions. The complexity is further increased owing to the interaction with turbulence. Besides, the injected liquid jet undergoes a continuous change of state from classical two-phase atomization, droplet formation and evaporation to a dense-fluid mixing phenomenon depending on the ambient pressure and temperature and the physical properties of the injected fuel. Indeed, experimental observations [48] of n-dodecane sprays after the end of injection have shown a dense-fluid mixing with vanishing surface tension as the ambient temperature and pressure exceed a certain limit. Besides, Crua et al. [16] observed that fuel droplets undergo a gradual transition from subcritical evaporation to dense-fluid mixing at pressures and temperatures higher than the pure fuel critical point, where the transition time depends on the pressure and temperature of the surrounding gas as well as the fuel properties. Accordingly, a CFD model capable of modeling the fuel injection under subcritical, transcritical, and supercritical regimes, allowing an automatic transition between the different regimes, remains a challenge addressed by the proposed model in the current work.

Several spray modeling approaches can be found in the literature, with varying complexity of describing the involved physical processes. The widely used spray model for engineering calculations is based on the Discrete Droplet Model (DDM) approach [24], where the liquid phase is described by Lagrangian parcels (i.e. a group of droplets with identical properties, such as diameter and velocity), whereas the gas-phase is modeled in an Eulerian framework. Several researchers [65, 30, 76, 46, 37] have adopted the DDM approach for spray simulations. These simulations have shown the effectiveness of this approach to describe the spray dynamics under turbulent conditions. However, as reported in [77, 12, 31], this approach also presents various shortcomings, especially to model the dense near-nozzle region, where parcels/blobs are injected to represent the intact liquid core. In addition, this modeling approach requires various calibration coefficients of submodels, which are not universal. Recent developments [53, 54] have been also carried out in the literature for using the DDM model within the dense regimes.

On the other hand, Eulerian modeling of fuel injection and atomization, where both the liquid and gas phases are treated in an Eulerian framework is more suited to model

the dense near-nozzle region. For instance, Interface Capturing Methods (ICM) such as the Volume of Fluid (VOF) [33] and Level-Set (LS) [69] methods have been applied to simulate the fuel injection and atomization [50, 68, 32]. However, due to the high computational cost of these methods, their application to industrial cases is still limited. Accordingly, another alternative is the Eulerian Diffuse Interface Model (DIM), where the unresolved interface features are modeled using a surface density approach instead of being tracked. Several atomization models have been proposed within the Eulerian framework based on the surface density approach as initially introduced by (Vallet and Borghi [72], Vallet et al. [73]) in the so-called $(\Sigma - Y)$ model. This model has two main transport equations: liquid fraction (Y) transport equation to track the liquid-phase dispersion and the interfacial surface area density (Σ) transport equation to model the unresolved liquid-gas interface, where the surface area density provides a general description of the atomized liquid structures such as droplets or ligaments. The liquid fraction and surface density can be used to estimate an equivalent Sauter Mean Diameter (SMD) defined as, $(SMD = 6\alpha_l/\Sigma)$, where $(\alpha_l = \rho Y/\rho_l)$ is the liquid volume fraction.

The known spray SMD may then be used to initiate a Lagrangian description of the spray when it becomes sufficiently diluted, as proposed in the Eulerian-Lagrangian Spray Atomization (ELSA) model [13, 44]. The Lagrangian description of the spray is indeed more appropriate for modeling the diluted spray region, allowing to track individual droplet's velocity, size, and temperature, in contrast to the Eulerian approach, which assumes a single temperature and velocity for both the droplets and the gas phase, and can't consider spray polydispersity, making it unsuitable to model such dispersed spray region. Similar to the ELSA approach, Devassy et al. [23] proposed an Eulerian-Eulerian atomization model using two surface density transport equations to separately model the liquid core atomization and droplet's secondary breakup. A Probability Density Function (PDF) based formulation of the $\Sigma - Y$ or ELSA model has also been proposed in [70, 9], where a joint PDF of liquid volume fraction and surface density is used to consider the subgrid fluctuations of these two scalars.

The potential of the $(\Sigma - Y)$ model to capture the fuel dispersion and atomization under diesel-like operating conditions, namely the ECN Spray A non-evaporating condition [2], has been shown in recent studies within the Reynolds Average Navier-Stokes (RANS) [20, 55] and Large Eddy Simulation (LES) [22, 10] frameworks. Besides, the LES-based formulations of the $(\Sigma - Y)$ model have demonstrated superior performance to their RANS counterpart in capturing the fuel dispersion in the near-nozzle field [22, 10].

However, such above models (see [10] for instance) commonly assume constant fluid properties or rely on a simple equation of state (EoS) to model the liquid and gas phases. Besides, the phase change is usually neglected or considered using simple evaporation models that don't incorporate the essential real-fluid effects relevant to high temperature and pressure injection. Under these conditions, the fuel properties show significant deviation from the ideal-gas behavior, where a real-fluid (EoS) is needed to capture the non-linear behavior of the fluid properties, especially under transcritical conditions [36, 35]. Lacaze et al. [43] also demonstrated the importance of real-gas effects in the simulation of the ECN Spray A evaporating condition [8] (high temperature and pressure condition) using the Peng-Robinson (PR) EoS.

In addition, for considering phase change, the EoS is insufficient, and vapor-liquid equilibrium (VLE) calculations are also required. Indeed, Matheis and Hickel [49] proposed a two-phase flow model using a thermodynamic model based on the PR-EoS and VLE calculations, applied to the simulation of the evaporating ECN Spray A. Yang et al.

[79] proposed a multi-component two-phase flow model, where the flow solver is coupled to a VLE solver also based on the PR-EoS. The model accuracy has been validated for the simulation of flash boiling cases [80], cavitation cases [78], and the evaporating ECN Spray A [79]. However, it has been found that the direct evaluation of the VLE calculation during the simulation run-time is computationally demanding, especially when employing a complex real-fluid (EOS) [78, 79]. Accordingly, a more robust and efficient tabulation approach could be one remedy for the computationally demanding VLE solver.

Several contributions to spray injection modeling using Eulerian two-phase flow models closed by tabulated real-fluid thermodynamics have been reported in the literature. A tabulated thermodynamic approach based on the Perturbed Chain Statistical Associating Fluid Theory (PC-SAFT) EoS has been proposed by Koukouvinis et al. [41] and applied to the evaporating ECN Spray A simulation. Jafari et al. [35] proposed an efficient tabulation approach to investigate the cryogenic injection of liquid nitrogen co-axially injected with hot hydrogen into supercritical nitrogen. The latter model is further used to explore the interaction between phase separation and turbulent fluid dynamics for *n*-hexane injection into supercritical nitrogen [36]. Moreover, the proposed thermodynamic tabulation approach [35, 36] has been further developed to handle ternary mixtures and applied to investigate fuel droplet evaporation under high-pressure dual-fuel conditions [27]. The aforementioned studies have proved that the tabulation approach can be efficient and reliable, especially for complex cases, allowing for significant savings in terms of computational cost. However, the storage memory requirements for the tables may become an issue as the table dimensions are extended for multi-species systems. Recently, other alternatives to the tabulation approach have also been proposed, such as using artificial neural network (ANN) as a regression model for the thermodynamic properties [42] or an in situ adaptive tabulation (ISAT) approach [82]. However, these approaches are still under investigation, and their efficiency for multi-component problems is not yet evaluated.

Based on the above discussion, the current study proposes a more generalized approach based on an efficient Eulerian diffuse interface two-phase real-fluid model (RFM) [27, 36, 35] that can represent the coexistence of multi-component subcritical and supercritical thermodynamic states and allows a smooth transition between the different thermodynamic regimes. The RFM model is a fully compressible multi-component two-phase model closed by a thermodynamic equilibrium tabulation method. The thermodynamic table is generated using the in-house IFPEN Carnot library based on VLE calculations coupled with a real-fluid EoS. In the current study, the RFM model is supplemented with a surface density transport equation within the LES framework to the model the fuel jet primary atomization under diesel-like operating conditions.

The proposed model is assessed using the non-evaporating and nominal (evaporating) conditions of the ECN Spray A injector [8]. Under the non-evaporating condition, the ECN experimental database includes near-nozzle fuel dispersion and interfacial surface area measurements by means of X-ray radiography [40] and ultra small-angle X-ray scattering (USAXS) technique [38], respectively. Besides, the SMD experimental data [38] are also used for model validation. On the other hand, under the nominal evaporating Spray A condition, model validation is carried out against experimental measurements of liquid and vapor penetrations [11] and fuel mixture fraction distribution [59, 6]. Compared to previous work [79] from the author's group for the evaporating ECN Spray A simulation, the computational efficiency and accuracy of the proposed tabulated RFM model as a remedy to the direct evaluation of costly phase equilibrium solver have been confirmed.

The current paper is organized as follows: Section 2 describes the RFM model, including the transport equations and the thermodynamic tabulation approach. Section 3 presents the test case setup and the RFM model validation against the ECN experimental database under non-evaporating and evaporating conditions. Finally, Section 4 summarizes the main conclusions along with the future perspectives.

2 The real-fluid model (RFM) description

2.1 Governing equations

The diffused interface two-phase flow model adopted in the current study is a four equation model that is fully compressible and considers multi-component in both phases under the assumptions of thermal and mechanical equilibrium. Within the LES framework, the filtered set of governing Equations (2.1-2.4) expresses the conservation of mixture mass, mixture momentum, mixture internal energy, and species mass fraction, respectively.

$$\frac{\partial \bar{\rho}}{\partial t} + \frac{\partial \bar{\rho}\tilde{u}_i}{\partial x_i} = 0 \tag{2.1}$$

$$\frac{\partial \bar{\rho}\tilde{u}_i}{\partial t} + \frac{\partial \bar{\rho}\tilde{u}_i\tilde{u}_j}{\partial x_j} = -\frac{\partial \bar{P}}{\partial x_i} + \frac{\partial}{\partial x_j}(\bar{\tau}_{ij} + \bar{\tau}_{ij}^{sgs}) \tag{2.2}$$

$$\frac{\partial \bar{\rho}\tilde{e}}{\partial t} + \frac{\partial \bar{\rho}\tilde{u}_j\tilde{e}}{\partial x_j} = -\bar{P}\frac{\partial \tilde{u}_j}{\partial x_j} + (\bar{\tau}_{ij} + \bar{\tau}_{ij}^{sgs})\frac{\partial \tilde{u}_i}{\partial x_j} + \frac{\partial}{\partial x_j}(\bar{q}_j + \bar{q}_j^{sgs}) \tag{2.3}$$

$$\frac{\partial \bar{\rho}\tilde{Y}_k}{\partial t} + \frac{\partial \bar{\rho}\tilde{u}_j\tilde{Y}_k}{\partial x_j} = \frac{\partial}{\partial x_j}(\bar{J}_{k,j} + \bar{J}_{k,j}^{sgs}) \tag{2.4}$$

where (ρ, u_i, P, e) denote the mixture's density, velocity vector, pressure, temperature and specific internal energy, respectively. Here, (τ_{ij}) is the viscous stress tensor and (q_j) is the heat flux. $(Y_k, J_{k,j})$ are the mass fraction and diffusion flux of species k, respectively. The subgrid scale contributions in the governing equations are indicated by the superscript (sgs).

The viscous stress tensor (τ_{ij}) is given by:

$$\tau_{ij} = \mu\left(\frac{\partial u_i}{\partial x_j} + \frac{\partial u_j}{\partial x_i} - \frac{2}{3}\frac{\partial u_k}{\partial x_k}\delta_{ij}\right) \tag{2.5}$$

where (μ) is the dynamic viscosity and (δ_{ij}) is the Kronecker-Delta.

The heat flux (q_j) consists of heat conduction calculated based on Fourier's law plus the enthalpy flux by species diffusion,

$$q_j = \lambda\frac{\partial T}{\partial x_j} + \rho D\sum_k h_k\frac{\partial Y_k}{\partial x_j} \tag{2.6}$$

where (λ) is the thermal conductivity, (T) is the temperature, (D) is the mass diffusion coefficient, and (h_k) is the specific enthalpy of species k, respectively. Here, (D) is assumed species independent and deduced from a given molecular Schmidt number (Sc) as $(D = \mu/\rho Sc)$. The dynamic viscosity and thermal conductivity are computed using Chung et al. [15] correlations.

The species diffusion flux $(J_{k,j})$ is modeled according to Fick's law:

$$J_{k,j} = \rho D\frac{\partial Y_k}{\partial x_j} \tag{2.7}$$

The subgrid stress tensor (τ_{ij}^{sgs}) is computed similarly to (τ_{ij}), with the eddy-viscosity assumption, replacing the molecular dynamic viscosity by the subgrid-scale dynamic viscosity $(\mu_{sgs} = \rho\nu_{sgs})$. The LES Sigma turbulence model [52] is used to compute the subgrid-scale kinematic viscosity, (ν_{sgs}) as follows,

$$\nu_{sgs} = (C_m \Delta)^2 D_m \, , D_m = \frac{\sigma_3(\sigma_1 - \sigma_2)(\sigma_2 - \sigma_3)}{\sigma_1^2} \tag{2.8}$$

where ($C_m = 1.5$) is the model constant and ($\Delta = V_c^{-1/3}$) is the filter size estimated from the cell volume (V_c). The differential operator (D_m) is computed from the singular values (σ_i) of the resolved velocity gradient tensor with ($\sigma_1 \geqslant \sigma_2 \geqslant \sigma_3 \geqslant 0$), as detailed in [52].

The subgrid species ($J_{k,j}^{sgs}$) and heat (q_j^{sgs}) fluxes are modeled using the gradient assumption, where the molecular transport coefficients in ($J_{k,j}$) and (q_j) are replaced with the turbulent ones. The turbulent transport coefficients (D_t, λ_t) are modeled by introducing a turbulent Prandtl ($Pr_t = 0.9$) and Schmidt ($Sc_t = 0.7$) numbers as:

$$D_t = \frac{\mu_{sgs}}{\rho Sc_t} \, , \lambda_t = \frac{C_p \mu_{sgs}}{Pr_t} \tag{2.9}$$

where (C_p) is the isobaric heat capacity.

The liquid jet atomization is modeled by solving a transport equation for the evolution of the interfacial surface area density (Σ), which is defined as the liquid-gas interfacial area per unit volume. The adopted (Σ) equation within the LES framework is based on the proposal by Chesnel et al. [14], where the total interfacial surface area is given by:

$$\Sigma = \Sigma_{min} + \Sigma^{'} \tag{2.10}$$

where the (Σ_{min}) represents the minimum surface density that can be found for a given value of the resolved liquid volume fraction, whereas ($\Sigma^{'}$) stands for the subgrid level surface density. The (Σ_{min}) is computed following [14] as:

$$\Sigma_{min} = \frac{2.4}{\Delta_{LES}} \sqrt{\bar{\alpha}_l (1 - \bar{\alpha}_l)} \tag{2.11}$$

where (Δ_{LES}) is the filter length scale, which is estimated from the cell volume (V_c) as ($\Delta_{LES} = V_c^{-1/3}$) and ($\bar{\alpha}_l$) is the resolved liquid volume fraction.

To close Eq. 2.10, the subgrid surface density ($\Sigma^{'}$) is transported as follows:

$$\frac{\partial \Sigma^{'}}{\partial t} + \frac{\partial \tilde{u}_i \Sigma^{'}}{\partial x_i} = \frac{\partial}{\partial x_j} \left(D_\Sigma \frac{\partial \Sigma^{'}}{\partial x_j} \right) + \frac{\Sigma}{\tau_\Sigma} \left(1 - \frac{\Sigma}{\Sigma_{eq}} \right) \tag{2.12}$$

On the RHS of Eq. 2.12, the first term represents the turbulent diffusion flux modeled using a gradient law closure [45], where the diffusion coefficient (D_Σ) is computed as ($D_\Sigma = \mu_{sgs}/\rho Sc_t$). The second term on the RHS of Eq. 2.12 represents the surface production/destruction, due to turbulent flow stretching and coalescence effects, which is modeled in a restoration to equilibrium form [73, 45], where (Σ_{eq}) is an equilibrium surface area density that should be reached within a characteristic time scale (τ_Σ). The time scale (τ_Σ) is related to the turbulent time scale (τ_t) by the coefficient (C_Σ) as:

$$\frac{1}{\tau_\Sigma} = \frac{C_\Sigma}{\tau_t} \tag{2.13}$$

The (Σ_{eq}) is evaluated as ($\Sigma_{eq} = \Sigma_{min} + \Sigma_{eq}^{'}$), where ($\Sigma_{eq}^{'}$) is computed as function of a critical Weber number (We_c) [25] as:

$$\Sigma_{eq}^{'} = 4 \frac{0.5(\rho_l + \rho_g)\bar{\alpha}_l(1 - \bar{\alpha}_l)k_{sgs}}{\sigma We_c} \tag{2.14}$$

where (k_{sgs}) is the subgrid scale turbulent kinetic energy, (σ) is the surface tension coefficient computed by the Macleod-Sugden correlation [63] for the considered binary system of (n-dodecane/nitrogen), and (ρ_l, ρ_g) are the densities of the liquid and gas phases, respectively. In the validation section below, the two model constants (C_Σ, We_c) are set by comparison with the USAXS experimental measurements of the projected interfacial surface area.

A length scale (l_{32}) can be defined for the liquid structures from (Σ) and (α_l) following [10] as:

$$l_{32} = \frac{6\alpha_l(1-\alpha_l)}{\Sigma} \tag{2.15}$$

This length scale definition considers on the one hand, the case of monodispersed spray of spherical droplets ($SMD = 6\alpha_l/\Sigma$) and on the other hand, the case tending to a bubbly flow ($SMD = 6(1-\alpha_l)/\Sigma$).

It is worth noting that in the current proposed model, the overall liquid volume/mass fraction is not directly transported as in previous ($\Sigma - Y$) or ELSA models, but the liquid volume fraction (α_l) is one of the VLE calculation results and obtained from the stored thermodynamic table as a function of (T, P, Y_k). Accordingly, the phase change effect on the surface density is implicitly considered through the terms (Σ_{min}) and (Σ_{eq}), which are dependent on (α_l). Besides, the variation of the properties ($\rho_l, \rho_g, \sigma, ..., etc$) involved in the ($\Sigma$) equation depends on the local conditions of (T, P, Y_k) as provided by the thermodynamic table and discussed in the next section.

Another essential point regarding the function of the surface density (Σ) in the current model is that (Σ) here is a passive scalar, which is mainly used to compute the droplet's SMD distributions during the simulation. The surface density (Σ) is thus not fed back into Equations (2.1-2.4), as the liquid dispersion is assumed to be mainly governed by turbulent diffusion of the injected fuel (i.e., the n-dodecane species) through Equation (2.4) and independent of the atomization dynamics under the considered diesel-relevant conditions (high ambient density and injection pressure). However, the accuracy of such passive (Σ) formulation is diminished under conditions of lower ambient density and injection pressure, where the slip velocity between the droplets and the gas phase becomes more significant [29, 56]. An enhanced formulation has been recently proposed in [56] to overcome this limitation. The proposed model considered the diffusion due to the slip velocity between phases, allowing coupling between liquid dispersion and spray atomization, as (Σ) actively affects the transport of the liquid fraction. The enhanced model showed improved predictions under conditions of low ambient density and injection pressure. However, the enhanced model improvements were limited under high ambient density and injection pressure conditions.

The employed assumptions in the current modeling approach are summarized in the following points:

- The injected liquid operates at high Reynolds and Weber numbers.
- The two phases are in mechanical and thermal equilibrium.
- The fluid within a computational cell is in local thermodynamic equilibrium.

The first assumption allows to assume that large scale flow features such as mass transport are separated from the atomization process occurring at smaller scales. Accordingly, Equations (2.1-2.4) describe the large-scale motion of the flow and the atomization occurring at smaller scales is modeled by the surface density equation. In addition, the

high Weber number implies that surface tension has negligible effect on large scales, however its effect on the atomization is considered through the surface density equation. The second assumption implies that the two-phases are assumed to have a single velocity, pressure and temperature. Thus, the slip velocity between the two-phases is assumed to be not significant. Such assumption loses its validity under lower injection pressure and ambient gas to liquid density ratio, where the slip velocity becomes more significant [29]. This limitation could be overcome by adding a transition to the Lagrangain approach once the spray is diluted [13, 44] or accounting for the liquid diffusion due to the slip velocity [56]. The third assumption implies that the characteristic time of reaching local thermodynamic equilibrium is much smaller than the other flow time scales. Accordingly, thermodynamic non-equilibrium effects are not considered. However, the validity of the thermodynamic equilibrium assumption for high injection pressure diesel sprays has been demonstrated in previous studies [81, 49, 79], and will be further verified in the current study.

2.2 Tabulated thermodynamic closure

The fully compressible multi-component two-phase flow system described above is closed by a real-fluid EoS adopting a local thermodynamic equilibrium hypothesis, ensuring its mathematical hyperbolicity [80]. The validity of the thermodynamic equilibrium assumption for high injection pressure diesel sprays has been demonstrated in previous studies [81, 49, 79], which justifies its employment in the current study. To consider the phase change phenomenon, the EoS is not sufficient, but VLE calculations are also included in the current study.

In this work, the thermodynamic closure is obtained using the Peng–Robinson EoS [58] formulated as:

$$P = \frac{RT}{v-b} - \frac{a(T)}{v\,(v+b) + b\,(v-b)} \tag{2.16}$$

where (R) is the ideal gas constant, (T) is the temperature, (v) is the molar volume. The energy parameter $(a(T))$ and co-volume parameter (b) are computed for pure component i as:

$$\begin{gathered} a_i(T) = (a_0)_i \left[1 + (c_1)_i \left(1 - \sqrt{\tfrac{T}{T_{c_i}}}\right)\right]^2 \\ (a_o)_i = 0.45724 \tfrac{R^2 T_{c_i}^2}{P_{c_i}},\ (c_1)_i = 0.37464 + 1.5422\omega_i - 0.26992\omega_i^2 \end{gathered} \tag{2.17}$$

$$b_i = 0.07780 \frac{RT_{c_i}}{P_{c_i}} \tag{2.18}$$

where (T_{c_i}) is the critical temperature, (P_{c_i}) is the critical pressure, and (ω_i) is the acentric factor for each pure component i. Besides, when the PR EoS is used for mixtures, Van-der Waals mixing rules are applied for the energy and co-volume parameters $(a(T), b)$ as:

$$\begin{gathered} a(T) = \textstyle\sum_i \sum_j x_i\, x_j \sqrt{a_i(T) a_j(T)}\,(1 - k_{ij}) \\ b = \textstyle\sum_i x_i\, b_i \end{gathered} \tag{2.19}$$

where (x_i) is the molar fraction of component i and (k_{ij}) is the binary interaction parameter that can be fitted to experimental data to well represent the phase diagram of a binary system. In addition, volume translation [18] of the PR-EoS has been employed to improve the accuracy of the liquid density predicted by the cubic PR-EoS (see Appendix A.2). As such, the volume-translated PR-EoS is termed below as (VTPR-EOS). It is also worth noting that volume translation does not influence the predicted phase equilibrium conditions. Another important point related to employing a real-fluid EoS for the LES of turbulent flows is that subgrid-scale (SGS) models for the real-fluid EoS could be required, as recently highlighted in [71]. Such subgrid-scale models are not yet included in the current model, and thus quantification of the associated uncertainties are subject of future studies.

The current work adopts a pre-tabulation approach, where before the CFD simulation, a thermodynamic table is generated using the in-house IFPEN-Carnot thermodynamic library. The thermodynamic library performs the VLE calculation using a robust isothermal-isobaric (TP) flash [51] based on the real-fluid VTPR-EOS. The tabulated properties include the thermodynamic equilibrium density, internal energy, liquid volume fraction, fluid-phase state, and composition, and necessary thermodynamic derivatives as heat capacity, sound speed, and transport properties, as described in Appendix A.2.

The thermodynamic table inputs are the temperature (T), pressure (P), and species mass fraction ($Y_k, k = 1, N_s - 1$,where N_s is the total number of species). This tabulation approach offers the advantage of avoiding the direct evaluation of the non-linear real-fluid EoS along with the VLE calculation during the simulation, which has been proven to be computationally demanding [79, 80]. Moreover, the tabulation approach based on the IFPEN-Carnot thermodynamic library allows simulating different fuels/species using different EoSs without hard coding a (TPn) flash for each EoS of interest. During the simulation, the tabulated quantities are interpolated using the inverse distance weighting method (IDW) [74]. The thermodynamic table is coupled with the CONVERGE CFD solver [66] as detailed in [35, 27, 36].

The thermodynamic table is used during the simulation for two main tasks as follow:

- Properties look-up: compute the thermodynamic and transport properties, phase state, and composition from ($T, P, Y_k, k = 1, N_s - 1$) obtained by the flow solver.
- Temperature reverse look-up: compute the temperature from the ($e, P, Y_k, k = 1, N_s - 1$) provided by the flow solver.

The accuracy of the VLE computation performed by the IFPEN-Carnot thermodynamic library using the VTPR-EOS has been validated for the (n-dodecane/nitrogen) binary mixture against published experimental data, as demonstrated in Appendix A.1. The obtained results have shown a satisfactory agreement with the experimental data, which demonstrates the reliability of the thermodynamic library along with the VTPR-EOS to accurately model the considered binary mixture. In addition, the calculation of pure components (n-dodecane and nitrogen) properties is validated against the NIST database [26] showing good agreement (see Appendix A.2).

3 Description of the simulated test cases

The current study is based on the ECN Spray A configuration [8], where a single-hole diesel injector is operated with pure n-dodecane ($C_{12}H_{26}$) injected into gaseous nitrogen (N_2) at

the conditions listed in Table 3.1, including non-evaporating and evaporating conditions. The test case setup is described in the next section, followed by the comparison of the RFM-LES results against the ECN experimental data. The ECN experimental database of the non-evaporating condition will be used to validate model results for the near-nozzle field, while the evaporating conditions experimental data will be used to validate the far-field spray.

Fuel	n-dodecane
Injection pressure (MPa)	150
Injection temperature (K)	$343^a/363^b$
Ambient temperature (K)	$303^a/900^b$
Ambient pressure (MPa)	$2^a/6^b$
Ambient density (kg/m^3)	22.8
Ambient composition	Pure N_2

Table 3.1: Injection and ambient conditions of ECN Spray A experiments under ^{a} Non-evaporating and ^{b} evaporating conditions.

3.1 Computational domain and model set-up

A three dimensional (3D) rectangular computational domain is used in the current study, which is 20 mm in the stream-wise direction and 10 mm in the lateral directions. The nozzle outlet diameter is 0.0894 mm corresponding to Spray A injector serial #210675 [1]. The grid structure at the domain center-plan is depicted in Fig. 3.1, where the base grid size is 400 μm located at the outer edge of the domain, while various mesh refinement levels have been employed to achieve a minimum cell size of $\backsim$ 6 μm. Thus, the nozzle outlet diameter is discretized with about 15 cells.

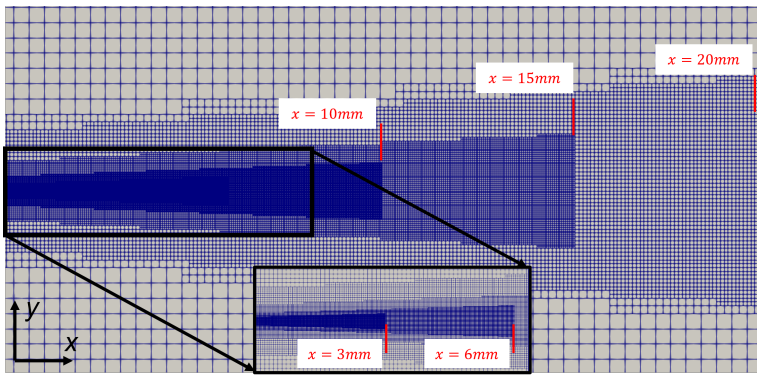

Figure 3.1: Computational domain with the grid structure at the domain central cut section, along with the length of the various embedding zones. The insert shows a zoom of the refined mesh in the near-nozzle exit region.

Grid convergence study has been performed, where three different grids have been tested. The minimum grid size for the three tested grids is fixed to 6 μm, located in the near nozzle region ($x < 3\,mm$). Then, the other embedding zones (see Fig. 3.1) are further refined from the coarsest grid to the most refined one, resulting in three grids with a total mesh count of 3 M (grid 1), 16 M (grid 2), and 21 M (grid 3) cells, respectively.

The injection conditions are applied at the domain inlet (the nozzle orifice exit) by an inlet boundary condition (BC). Thus, the injector in-nozzle flow is not simulated. The

inlet BC is prescribed as a top-hat (TH) profile of axial velocity calculated from the time-dependent mass flow rate profile obtained from CMT virtual injection rate generator [5], which allows to partially reproduce the in-nozzle flow and the needle motion effects [21].

Under both evaporating and non-evaporating conditions, simulations are first carried out without imposing any synthetic turbulence fluctuations at the domain inlet. However, under the non-evaporating condition, the obtained initial results have shown an overestimation of the jet penetration and less fuel dispersion compared to the experimental data. Thus, a synthetic turbulence generator has been used to superimpose turbulent fluctuations over the inflow velocity profile following the method by [17]. A turbulent intensity of 3% has been employed following the recent work of [22] and the minimum length-scale of the imposed fluctuations was taken as twice the minimum cell size. On the other hand, under the evaporating condition, preliminary simulation results have shown that the injected liquid jet penetration and dispersion behaves correctly without adding such synthetic turbulent fluctuations. Fairly accurate predictions of the evaporating Spray A without imposing any artificial turbulence at the inflow patch have been also shown in [49]. It seems that the interaction between the counter flows of gas entrainment and evaporation at the interface will trigger the jet instability, as suggested in [79]. Accordingly, future work should include the in-nozzle flow in the spray simulation to avoid such uncertainties on the inflow boundary conditions.

A no-slip boundary condition is applied at the wall around the nozzle outlet (on left side of the chamber). All the rest of the domain boundaries are outlets with a pressure boundary condition equal to the ambient pressure. LES simulations are carried out using the RFM model described above. The numerical solution of the transport equations is based on a modified Pressure Implicit with Splitting of Operator (PISO) algorithm [34] for the pressure-velocity coupling. The accuracy of the employed PISO algorithm under trans/supercritical conditions has been validated in the authors previous work [36, 35, 27] and will be further demonstrated in the results section under the considered conditions. The solution procedure of the governing equations using the PISO algorithm is summarized in Appendix A.3.

The spatial discretization is second-order accurate using a central difference scheme. The time integration is achieved by a second-order Crank-Nicolson scheme for the momentum equation and a first-order implicit Euler scheme for the rest of the equations. The time step is around 2-3 ns and adjusted automatically based on a maximum Courant-Friedrichs-Lewy (CFL) number of 0.5. As an example of the computational cost of the performed LES simulations, it required about 9 days to simulate 1 ms under the evaporating condition with grid 2 (16 M cells), using 1024 cores of AMD EPYC Milan 7763 processors running at 2.45 GHz (Topaze CCRT supercomputer).

The RFM model thermodynamic closure for the (n-dodecane/nitrogen) binary mixture is based on the VTPR-EoS with a uniform thermodynamic table resolution in $(T, P, Y_{C_{12}H_{26}})$ axes of $(501 \times 61 \times 101)$ points covering ranges of (300-1300 K, 1-121 bar, 0-1). The employed thermodynamic table resolution is based on previous studies [36, 27, 35], and will be shown to provide sufficiently accurate results in the following sections.

4 Non-evaporating ECN Spray A

4.1 Spray dispersion

The RFM model predictions of the spray dispersion is validated using the ECN experimental data [2], which include the projected mass density (PMD) [40], transverse integrated mass (TIM) [39], and liquid volume fraction (α_l) [60]. The LES results are time-averaged between 0.4 and 1 ms after the start of injection (during the quasi-steady period) to be compared with the experiments. A first validation is performed using the PMD, which represents a path length-integrated measure of the fuel density along the X-ray beam path through the spray depth. Line of sight integration of the simulation results of the fuel density is carried out and compared with the experimental data as shown in Fig. 4.1. The comparison shows that the simulation capture well the fuel distribution in the near-nozzle region (first 6 mm), where a qualitatively good agreement is achieved between the computed and measured PMD.

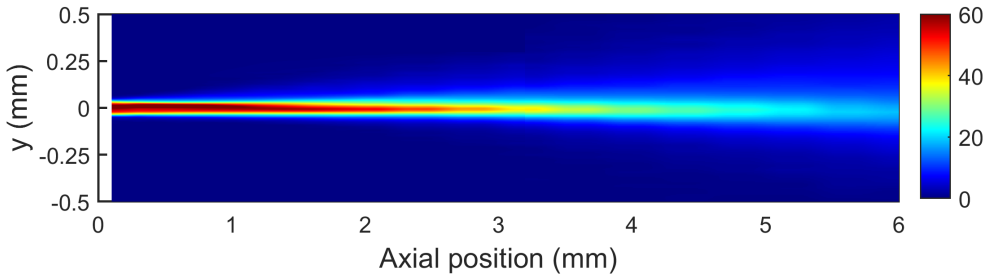

(a) ECN X-ray

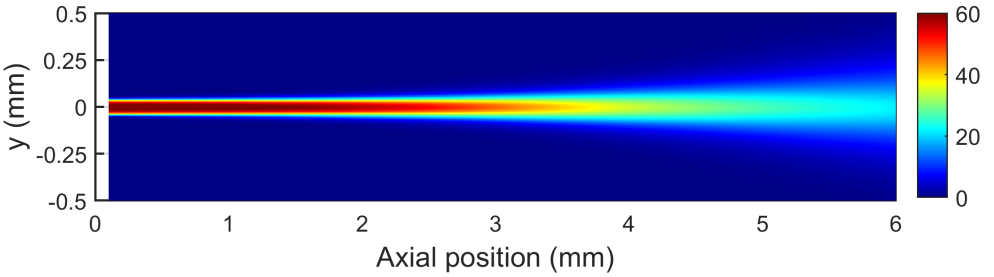

(b) LES-Grid 2

Figure 4.1: Non-evaporating Spray A condition: experimental (top) and numerical (bottom) projected mass density (µg/mm^2) distributions. (color online)

In addition, for more quantitative validation, the projected mass density radial profiles are compared at three different axial positions ($x = 0.1, 2, 6$ mm) from the nozzle outlet as depicted in Fig. 4.2. Overall, the model results are in good agreement with the experimental data in terms of the spray centerline peak-value and radial dispersion, especially when the grid 2 and 3 are employed.

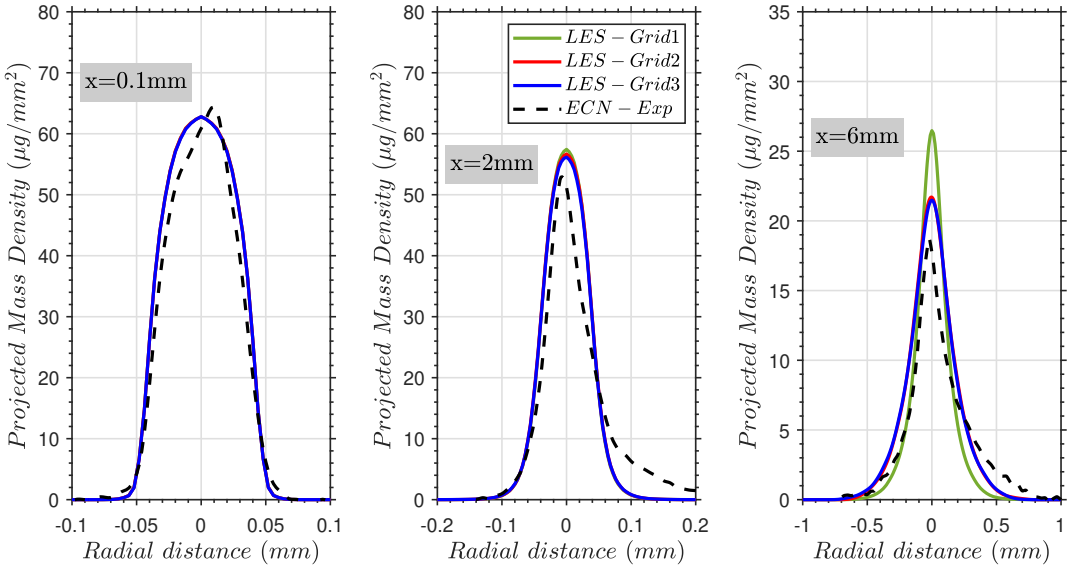

Figure 4.2: Non-evaporating Spray A condition: Numerical and experimental projected mass density (PMD) radial profiles at axial distances of 0.1 mm, 2 mm, 6 mm from the nozzle exit. The grid convergence study is also demonstrated. (color Online)

Indeed, it can be seen the grid impact on the obtained results, especially at ($x = 6$ mm), where the predicted PMD profile matches better the experimental one as the mesh is further refined (less overestimation of the peak value). Besides, a minimal variation of the obtained results can be observed as the grid is further refined from grid 2 (16 M cells) to grid 3 (21 M cells), showing that grid convergence is achieved. Thus, the intermediate grid resolution (grid 2- 16 M cells) has been used for further calculations, and the associated results are only shown in the following discussion.

In addition to the presented grid convergence study, the quality of the performed LES using (grid 2) is assessed based on the criterion proposed by Pope [64]. This criterion is satisfied when the ratio (M) of the subgrid-scale kinetic energy (k_{sgs}) to the sum of the modeled and resolved turbulent kinetic energy ($k_{sgs} + k_{res}$) is less than 20%, such that ($M = k_{sgs}/(k_{sgs} + k_{res}) < 0.2$). The time averaged ratio (M) at the center-plane of (grid 2) is depicted in Fig. 4.3, showing that ($M < 0.2$) is fairly accomplished within the spray limits (region of interest), identified by a time averaged liquid volume fraction iso-line of 0.15%. The carried out assessment shows that the employed grid resolution is sufficient to provide reliable results within the LES framework.

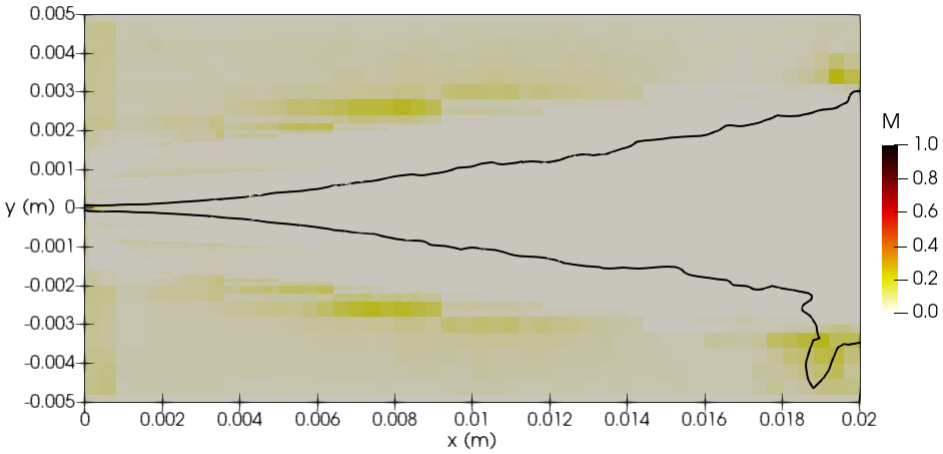

Figure 4.3: Non-evaporating Spray A condition: LES quality analysis based on the Pope criterion [64] : $(M = k_{sgs}/(k_{sgs} + k_{res}) < 0.2)$ for grid 2. The black iso-line of time averaged liquid volume fraction ($\alpha_l = 0.15\%$) shows the spray limits.

Another quantity used for validation is the TIM, obtained from the integral of the projected mass density across the radial direction at a particular axial location. Thus, a higher TIM value indicates a greater amount of liquid fuel along the radial direction. A comparison between the numerical and experimental TIM distributions is depicted in Fig. 4.4. The simulation result reasonably agrees with the experimental data in the first 5 mm. Then, the simulation overestimates the TIM as the axial distance increases, indicating that the PMD radial distribution is not accurately predicted at such axial positions (see PMD radial distribution at $x = 6$ mm in Fig. 4.2).

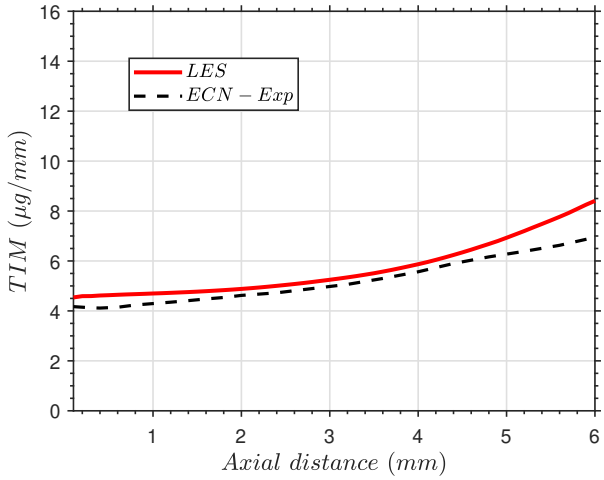

Figure 4.4: Non-evaporating Spray A condition: Numerical and experimental transverse integrated mass (TIM) along the spray axis.

In addition to the PMD and the TIM, the liquid volume fraction (α_l) distribution is also used for validation. The experimental data of liquid volume fraction is obtained by a tomographic reconstruction [60] of the X-ray radiography data. A comparison between the predicted and reconstructed liquid volume fraction distribution along the spray axis is shown in Fig. 4.5. It is worth noting that the experimental profile is only available in the first 12 mm. The comparison shows that the simulation result match with great

accuracy the experimental profile, reproducing the intact liquid core ($\alpha_l > 0.9$) and the liquid volume fraction decay along the spray axis. It also shows that the model can capture well the fuel dispersion from the dense near-nozzle region to more diluted zones of the spray.

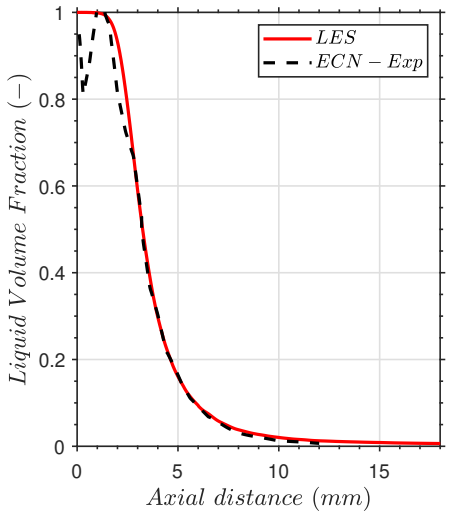

Figure 4.5: Non-evaporating Spray A condition: Numerical and experimental liquid volume fraction along the spray axis.

For a more detailed comparison, the numerical and reconstructed liquid volume fraction radial profiles are compared at three different axial locations similar to the PMD, as depicted in Fig. 4.6. The simulation results are in good agreement with the experimental profiles. The peak value at the spray center line is well captured by the model at ($x = 0.1, 6\,\text{mm}$), while overestimated at ($x = 2\,\text{mm}$), which is consistent with the liquid volume fraction distribution along the spray axis (see Fig. 4.5).

In summary, the performed assessment based on the projected mass density (PMD), transverse integrated mass (TIM), and liquid volume fraction experimental data shows that the RFM model can capture well the fuel dispersion with sufficient accuracy under the considered conditions.

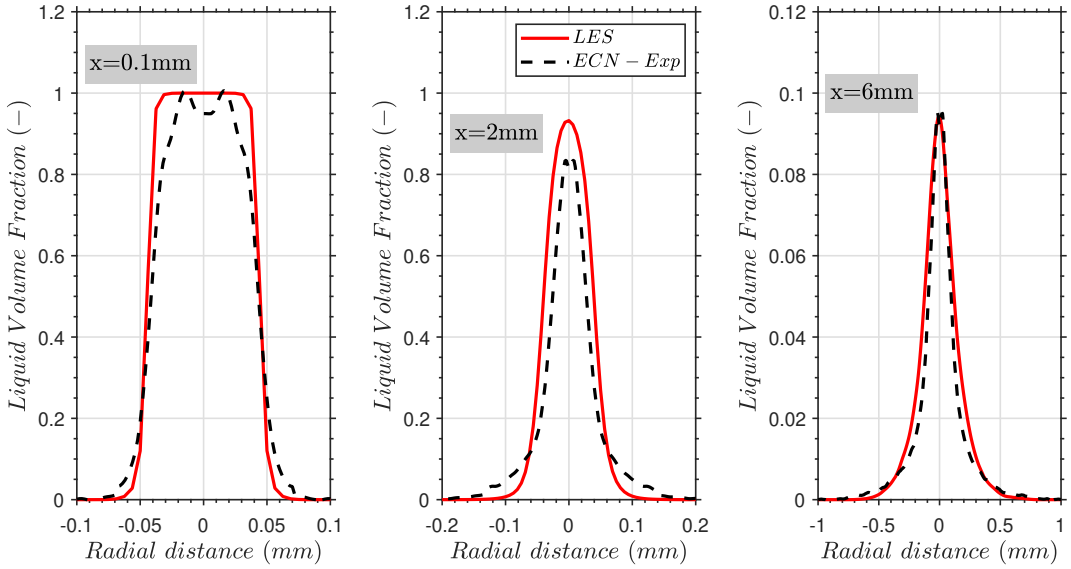

Figure 4.6: Non-evaporating Spray A condition: Numerical and reconstructed liquid volume fraction radial profiles at axial distances of 0.1 mm, 2 mm, 6 mm from the nozzle exit.

4.2 Spray atomization

The assessment of the proposed atomization model described above is carried out in the current section using the USAXS measurements of the projected interfacial surface area density [38, 55] and SMD experimental data [38]. It is worth recalling the surface density equation includes two modeling constants (C_Σ, We_c) that need to be calibrated against DNS or experimental data. The USAXS experimental data are used in the current work to fix the two model constants. The constant (C_Σ) is set by default to 1, as it has been shown in previous studies [22, 55], that a value in the vicinity of one is sufficient to match the experimental data. Regrading, the critical Weber number (We_c), two values $(1.5, 6)$ were assessed against the USAXS experimental data. The $(We_c = 1.5)$ is the value proposed in [19] based on two-phase DNS studies, while $(We_c = 6)$ is the result of a parametric variation carried out recently in [22]. The projected surface area density provided by the USAXS measurements represents the line-of-sight integrated interfacial area per X-ray beam area along the spray centerline. Thus, the time-averaged numerical surface area density is integrated along the spray depth to be compared with the experiments. The comparison of the numerical and experimental projected surface area density along the spray axis is shown in Fig. 4.7 for the different values of (We_c).

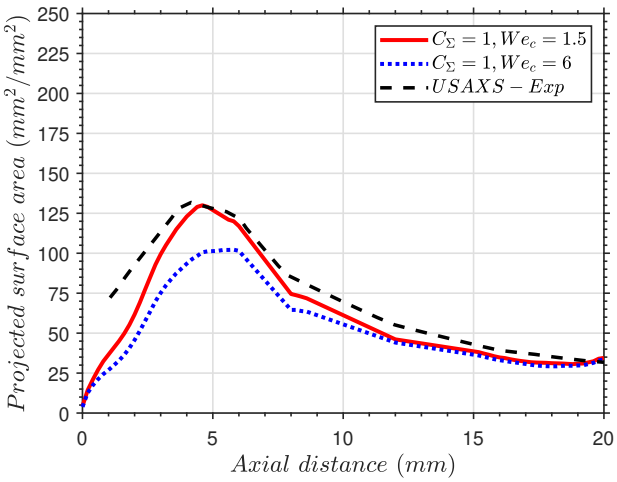

Figure 4.7: Non-evaporating Spray A condition: Numerical and experimental projected surface area along the spray axis.

Overall, the experimental surface area density is well reproduced by the model with ($We_c = 1.5$), whereas more deviation from the experimental data is found for ($We_c = 6$). Although some mismatches can still be observed with ($We_c = 1.5$), the model fairly recovers the experimental projected surface area peak value and decay along the spray centerline. The obtained results also highlight that some parameters tuning is still necessary in the current model for the surface density equation constants (C_Σ, We_c) to well reproduce the experimental surface area density. Thus, the model is still not completely free from parameter tuning, but indeed it is less number of parameters compared to classical Lagrangian spray modeling approaches.

Simulation results with ($C_\Sigma = 1, We_c = 1.5$) are also compared with available SMD measurements that are obtained by combining the X-ray radiography and the USAXS measurements [38]. A quantitative comparison of the SMD radial profiles between the simulation and the experimental data at different axial positions is depicted in Fig. 4.8.

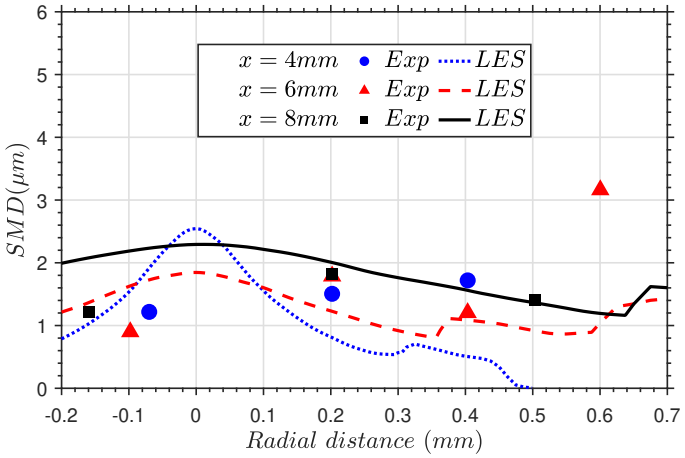

Figure 4.8: Non-evaporating Spray A condition: Numerical and experimental SMD radial profiles at axial distances of 4 mm, 6 mm, and 8 mm from the nozzle exit.

It can be observed that the drop sizes from the simulation fall into the same range as the experimental data. Besides, the simulation results tend to match better the experi-

mental data at longer axial distances from the nozzle exit, where the intact liquid core vanishes and the spray is more diluted, for instance at ($x = 8\,\mathrm{mm}$).

In Figure 4.9, the time averaged projected surface area radial profiles are shown at axial positions of 2 and 6 mm from the nozzle exit. It can be seen that at ($x = 2\,\mathrm{mm}$), the projected surface area profile exhibits two peaks at the jet periphery, with a minimum at the spray centerline. This minimum can be attributed to the presence of an intact liquid core at this axial position (see Fig. 4.5). Whereas at further downstream locations ($x = 6\,\mathrm{mm}$), the double-peak profile disappears, and a transition to a bell-shaped profile with a peak value at the spray centerline takes over, indicating the absence of an intact liquid core. This transition in the projected surface area profiles is similar to that reported by the USAXS experimental measurements for the ECN Spray D [12].

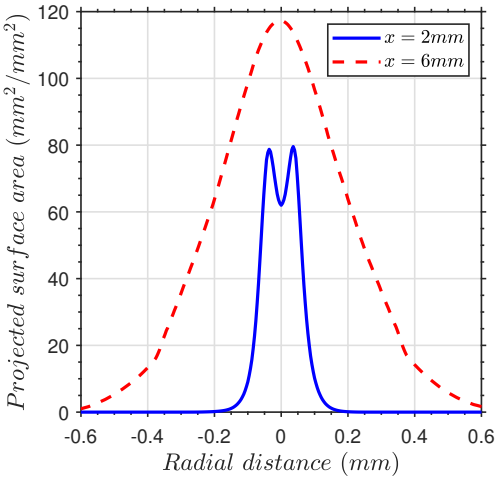

Figure 4.9: Non-evaporating Spray A condition: Numerical projected surface area profiles at axial distances of 2 mm and 6 mm from the nozzle exit.

5 Evaporating ECN Spray A

5.1 Comparison with experimental data

In the current section, the RFM model is further assessed under the nominal evaporating condition of the ECN Spray A (see Table. 3.1). Firstly, the temporal sequence of the n-dodecane injection in terms of mixture fraction at the grid center-plane is qualitatively compared against the experimental images taken by diffused back illumination (DBI) technique [47, 4], as depicted in Fig. 5.1. The blue isoline superimposed on the n-dodecane mixture fraction field demonstrates the liquid penetration with a liquid volume fraction ($\alpha_l = 0.15\%$).

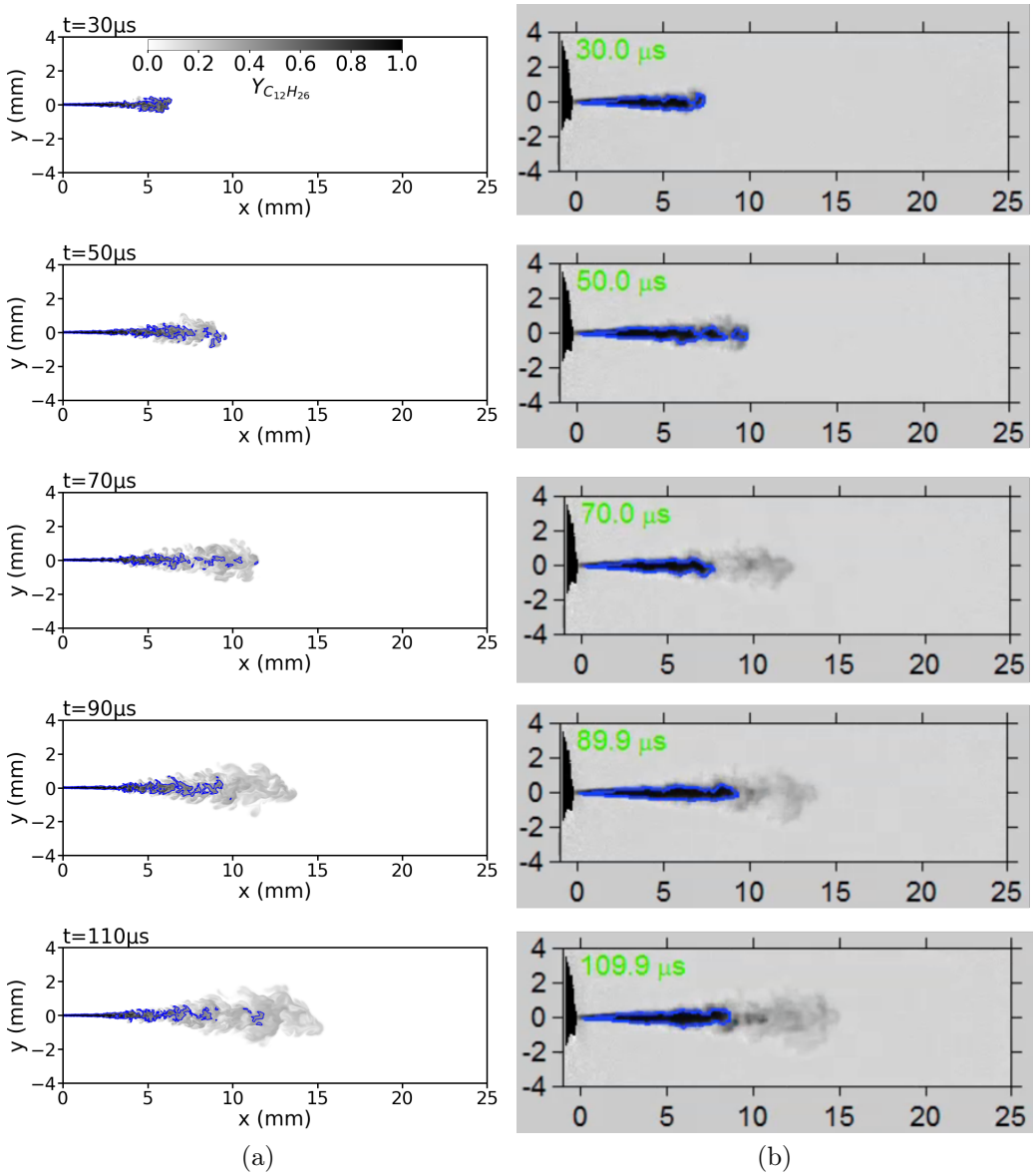

Figure 5.1: Evaporating Spray A condition: Temporal sequence of the n-dodecane injection. (a) LES results, (b) experimental data [47, 4]. Instantaneous n-dodecane mixture fraction distribution at the grid center-plane is presented for the LES results. The blue line superimposed on the LES results represents a liquid volume fraction (α_l) iso-line of 0.15%, which illustrates the liquid penetration length. (color online)

It can be observed the destabilization of the jet and the development of the instabilities at the shear layer, where liquid structures are detached from the liquid jet and further mix with the ambient gas. Overall, the simulation results show a good agreement with the experimental images with similar penetrations for both liquid and vapor at the various time instants.

A quantitative comparison of the spray penetrations between the LES results and the experimental data is shown in Fig. 5.2. The experimental data corresponds to liquid penetration obtained from diffused back illumination (DBI) [47] and Mie-Scattering [11, 7] techniques and vapor penetration obtained from Schlieren imaging [11, 7]. In the LES, the liquid penetration length is defined as $\max(x(\alpha_l = 0.15\%))$, where (x) is the axial distance

from the nozzle exit. The criterion to evaluate the liquid penetration length is based on the Mie-scattering theory analysis [61], where the (α_l) threshold value representing the liquid length was found to be ($\alpha_l < 0.15\%$) at Spray A condition. The vapor penetration length is defined as $\max(x(Y_{C_{12}H_{26}} = 0.1\%))$ as recommended by the ECN [3], where ($Y_{C_{12}H_{26}}$) is the n-dodecane mass fraction. It can be seen that the predicted liquid penetration matches well the experimental measurements, lying between the DBI and Mie scattering data. Besides, the predicted vapor penetration also fairly agrees with the experimental data.

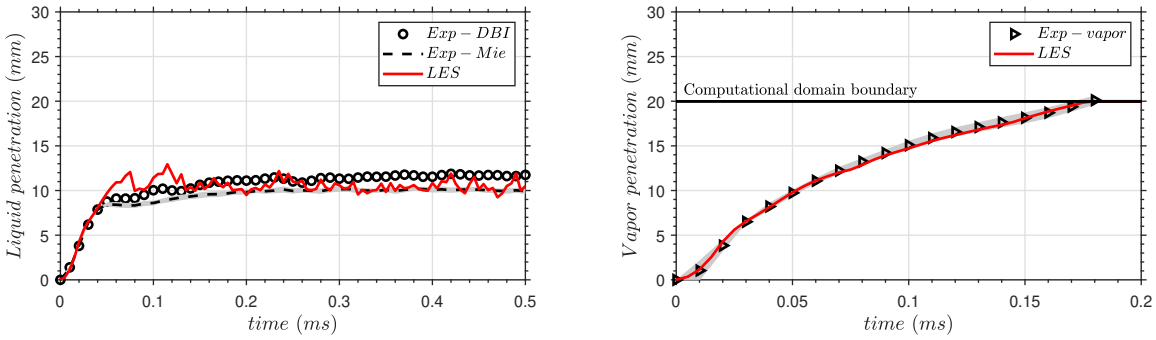

(a) (b)

Figure 5.2: Evaporating Spray A condition: Comparison of LES and experimental data for (a) liquid and (b) vapor penetration lengths. The experimental data corresponds to liquid penetration obtained from diffused back illumination (DBI) [47, 4] and Mie-Scattering [11, 7] techniques and vapor penetration obtained from Schlieren imaging [11, 7]. The shaded grey area represents the uncertainty in the experimental measurements.

In addition, the radial distribution of n-dodecane mixture fraction is compared between the simulation and the experimental data measured by Rayleigh scattering imaging [59, 6] as depicted in Fig. 5.3. The presented numerical result is obtained by time-averaging the LES results in the time interval between 0.4 and 1 ms after the start of injection (during the quasi-steady period). The shaded grey area in Fig. 5.3 represents 95% confidence interval in the experimental measurements. The simulation result agrees reasonably well with the experimental data within its confidence level. The predicted peak value on the jet axis tends to be slightly underestimated. However, the predicted mixture fraction decay along the radial direction is well captured compared to the experimental profile.

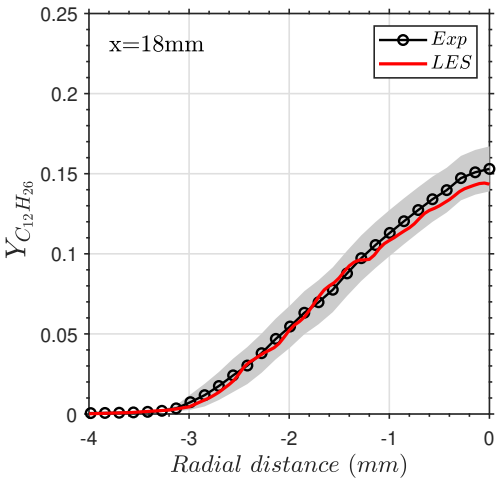

Figure 5.3: Evaporating Spray A condition: Numerical and experimental [59, 6] *n*-dodecane mixture fraction radial distribution at an axial distance of 18 mm from the nozzle exit. The shaded grey area represents 95% confidence interval in the experimental measurements.

5.2 Thermodynamic analysis and VLE model results

To further analyze the phase change and mixing processes, the temperature-composition phase diagram for the (*n*-dodecane-nitrogen) mixture at ($P = 6$ MPa) together with the adiabatic mixing temperature (T_{AM}) is shown in Fig. 5.4. The (T_{AM}) is formulated as,

$$h_{mix}(T_{AM}, P_{amb}, Y_{C_{12}H_{26}}) = Y_{C_{12}H_{26}}\, h_{C_{12}H_{26}}(T_{C_{12}H_{26}}, P_{amb}) + Y_{N_2}\, h_{N_2}(T_{N_2}, P_{amb}) \quad (5.1)$$

where $(h, Y_{C_{12}H_{26}}, Y_{N_2})$ are the specific enthalpy, the *n*-dodecane, and the nitrogen mass fractions, respectively. $(T_{C_{12}H_{26}}, T_{N_2}, P_{amb})$ denote the initial temperature of the fuel (*n*-dodecane), the initial temperature of the ambient N_2, and the ambient pressure, respectively. The adiabatic mixing temperature (T_{AM}) is computed considering the phase change based on the VLE solver. This is achieved by an offline iterative searching for the temperature (T_{AM}), such that the RHS of Equation 5.1 equals to the LHS, which represents the mixture's enthalpy evaluated from the VLE solver. The scattered data in Fig. 5.4 represents the thermodynamic states obtained from the LES simulation at $t = 110\mu s$.

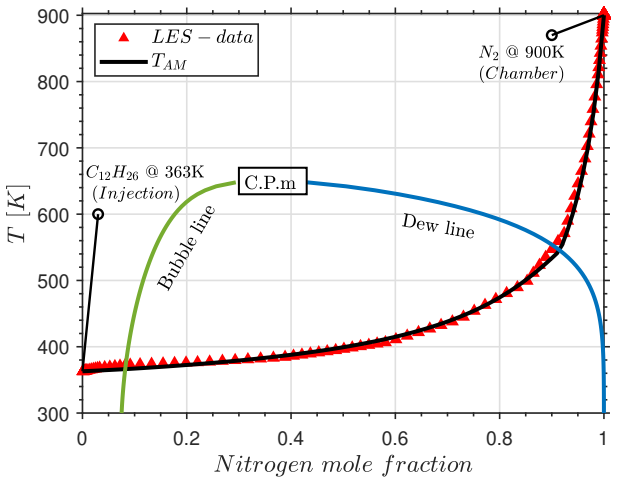

Figure 5.4: Evaporating Spray A condition: Temperature-composition diagram of $(C_{12}H_{26} - N_2)$ binary mixture at pressure of 6 MPa along with the adiabatic mixing temperature (T_{AM}) obtained offline from the VLE solver. The scattered data $(\triangle)$ represents the thermodynamic states from the LES simulation at $t = 110\mu s$. The two-phase region is bounded by the bubble line and the dew line, which intersect at the critical point of the mixture denoted by C.P.m.

The mixture temperature distribution from the LES is observed to follow well the adiabatic mixing temperature as a function of the N_2 concentration. In addition, the temperature distribution has crossed the two-phase region bounded by the bubble and dew lines. This confirms that subcritical phase transition occurs for the $(C_{12}H_{26} - N_2)$ binary mixture even at a pressure of 6 MPa, higher than the pure n-dodecane critical pressure $(P_{cr} = 1.8\,\text{MPa})$, as also demonstrated in previous studies [49, 79]. Indeed, the involved binary mixture may exhibit different thermodynamic regimes based on the local pressure, temperature, and species composition. Accordingly, it cannot be determined from an *a priori* analysis whether the Spatio-temporal variation of the involved thermodynamic states are subcritical or supercritical during the entire fuel injection event. As a matter of fact, both subcritical and supercritical regimes may exist simultaneously [79, 35, 36] in different locations of the chamber.

In addition to the previously discussed results, the employed VLE based model can provide valuable information regarding the phase change process and the composition of each species in each phase. The temporal evolution of the mass fractions of vaporous n-dodecane $(Y_{C_{12}H_{26},vap})$ and dissolved nitrogen in the liquid phase $(Y_{N_2,liq})$ are illustrated in Figs. (5.5a, 5.5b). The blue isoline of $(\alpha_l = 0.15\%)$ demonstrates the liquid penetration length. It should also be noted that within the employed LES framework and diffused interface model, artificial/numerical mixing could impact the obtained results. Accordingly, the results here of the mixing process should be interpreted while keeping in mind such numerical effects.

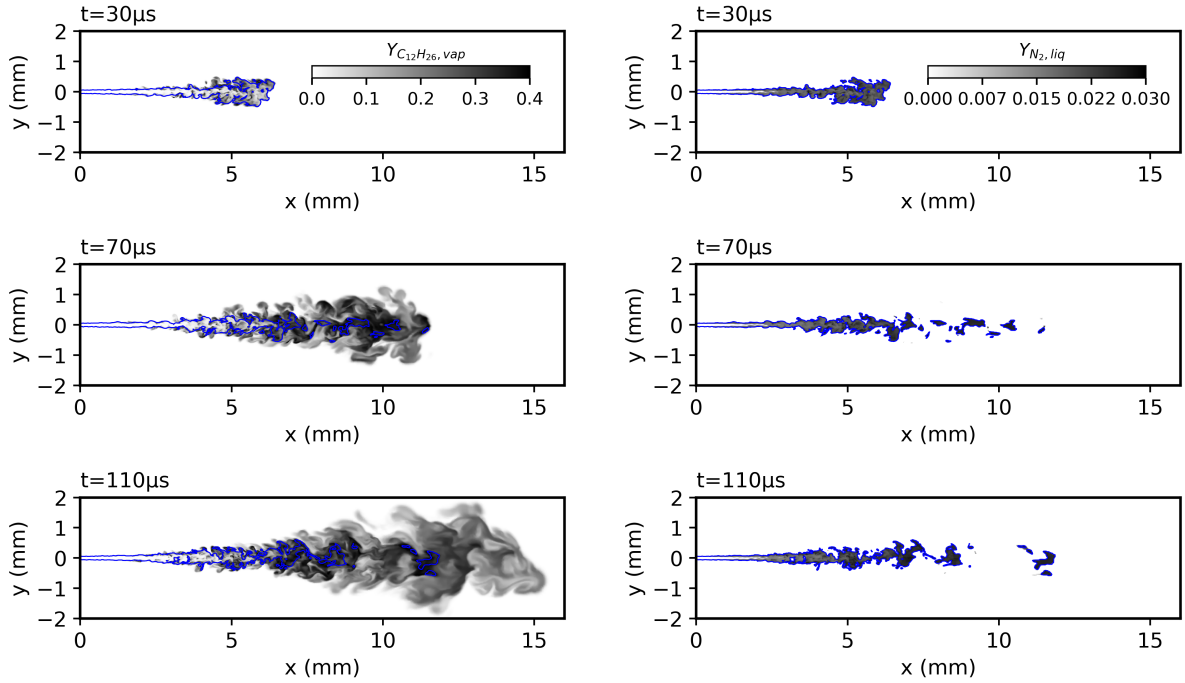

(a) (b)

Figure 5.5: Evaporating Spray A condition: Temporal evolution of the (a) mass fraction of vaporous n-dodecane ($Y_{C_{12}H_{26},vap}$) and (b) mass fraction of dissolved nitrogen in the liquid phase ($Y_{N_2,liq}$). The blue isoline illustrates the liquid penetration length based on the criterion ($\alpha_l = 0.15\%$). (color online)

It can be seen that the vaporous n-dodecane ($Y_{C_{12}H_{26},vap}$) is initially generated at the jet periphery with a significant accumulation at the jet tip, reaching a maximum of around 40%. Besides, a non-trivial amount of nitrogen is dissolved in the liquid jet, as shown in Fig. 5.5b, due to the enhanced solubility of the ambient gas in the liquid phase under the chamber high-pressure condition. One may also observe that the dissolved nitrogen in the liquid phase ($Y_{N_2,liq}$) increases sharply in the leading part of the liquid core and the atomized blobs, reaching a maximum of around 3%. This also demonstrates the role of the dissolution of non-condensable gases in the liquid phase as part of the phase change phenomenon.

Furthermore, the phase indicator (PHI) is depicted in Fig. 5.6, where ($PHI = 0, 1, 2$) denotes single liquid phase, single gas phase, and two-phase states, respectively. It can be seen that the jet exits the orifice with a single liquid phase state ($PHI = 0$) forming an intact liquid core, then as the jet travels in the chamber, it undergoes a transition to two-phase states ($PHI = 2$), due to the ongoing evaporation and mixing with the hot ambient gas. In addition, regions of single gas phase states ($PHI = 1$), where the vaporous n-dodecane exhibits a peak value can be observed (see Fig. 5.5a), indicating that the liquid n-dodecane is fully vaporized.

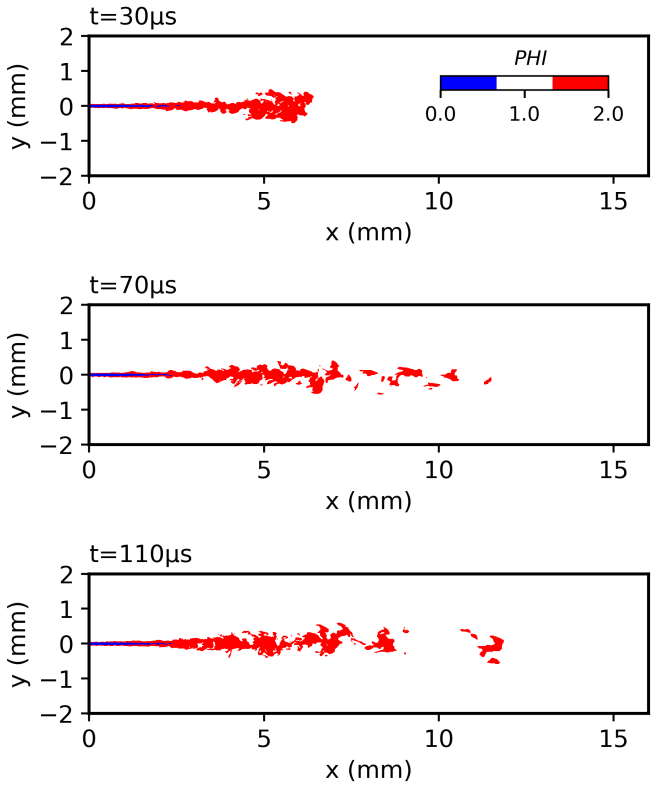

Figure 5.6: Evaporating Spray A condition: Temporal evolution of the phase indicator (PHI), where ($PHI = 0, 1, 2$) denotes single liquid phase, single gas phase, and two-phase states, respectively. (color online)

Further analysis is also carried out as an attempt to identify the distribution of the subcritical and supercritical states during the fuel injection event. For a multi-component mixture, the identification of the thermodynamic state (subcritical or supercritical) is not straightforward, as the mixture's critical point, which depends on the mixture's composition should be considered instead of the pure component's critical points. Here, a simplified criterion to identify subcritical and supercritical states for the considered binary mixture is used. Assuming that the mixing process takes place at a constant pressure equal to the chamber pressure (6 MPa), then the mixture critical temperature ($T_{cr,mix}$) can be identified from the temperature-composition diagram in Fig. 5.4. Accordingly, if the temperature exceeds the mixture's critical temperature, then the state is regarded as a supercritical state. Otherwise, the state is subcritical.

In Fig. 5.7, the temporal evolution of the reduced temperature ($T_r = T/T_{cr,mix}$) and gas volume fraction (α_g) distributions is shown. The vaporous n-dodecane mass fraction ($Y_{C_{12}H_{26},vap}$) distribution at the same time instants is also illustrated in Fig. 5.8. Only computational cells including mixture with nitrogen mole fraction (z_{N_2}) in the range of ($1e-03 < z_{N_2} < 0.999$) are illustrated. This is performed so that the pure or almost pure components regions are omitted. The black isoline of ($T_r = 1$) is also superimposed on the (α_g) and ($Y_{C_{12}H_{26},vap}$) contours.

At the early jet development ($t = 30\mu s$), the jet mainly exhibits a reduced temperature less than one. The vaporous n-dodecane mass fraction contours (see Fig. 5.8) also show that the formed fuel vapor is located inside the isoline of ($T_r = 1$), indicating that subcritical evaporation is taking place. As the jet further travels through the chamber and mixes with the hot ambient gas, more regions of ($T_r > 1$) can be observed (see

$t = 70, 110\mu s$). These regions correspond to locations composed of single gaseous-phase states (see α_g contours in Fig. 5.7) that have been heated to a temperature that exceeds the critical temperature of the mixture, reaching a supercritical state. At $(t = 70, 110\mu s)$, it can be also seen that the maximum mass fraction of the fuel vapor is located inside the $(T_r = 1)$ isoline, indicating that subcritical evaporation is the dominant phase-change process. This is consistent with the mixing path shown in Fig. 5.4, where the mixture has been through a large two-phase zone compared to much smaller single-phase zones.

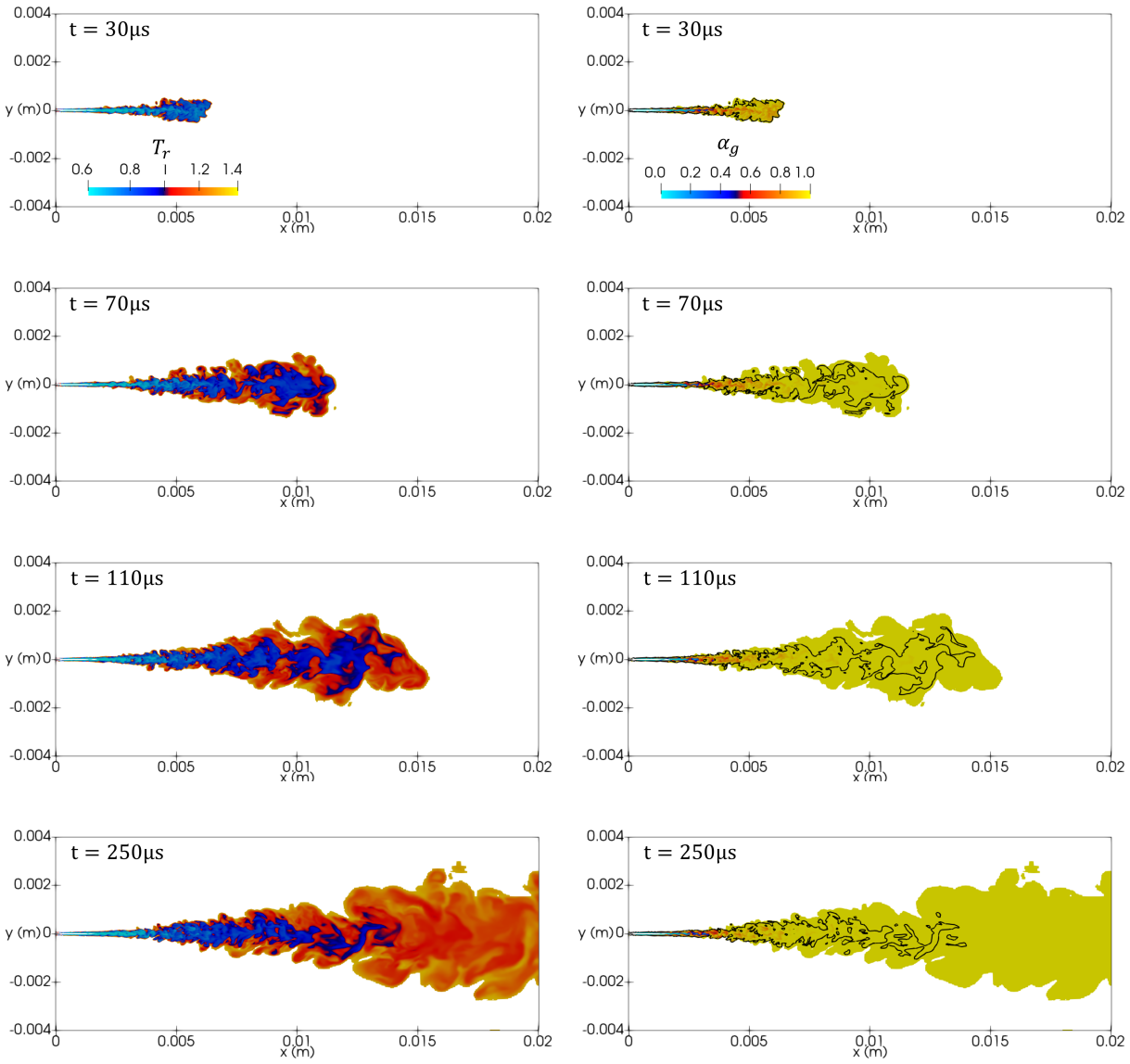

Figure 5.7: Evaporating Spray A condition: Temporal evolution of the reduced temperature ($T_r = T/T_{cr,mix}$) (left) and gas volume fraction (α_g) (right). Only cells with ($1e-03 < z_{N_2} < 0.999$) are shown. The black isoline on the (α_g) contours represents ($T_r = 1$) to illustrate the subcritical and supercritical regions.

Further, at $(t = 250\mu s)$, during the quasi-steady state injection period, it can be observed that the supercritical regions with $(T_r > 1)$ are more concentrated in the diluted spray locations. The contours of the reduced temperature again confirm that both sub-

critical and supercritical states may exist simultaneously during the fuel injection event under the considered conditions, and the transition from subcritical evaporation to single-phase diffusive mixing can be handled by the proposed model. It should also be noted that the presented analysis is an approximation as the pressure is generally not constant in the computational domain during the entire fuel injection event, but it fluctuates, especially during the early injection phase. Thus, the critical condition is not constant, as adopted here in the current simplified analysis.

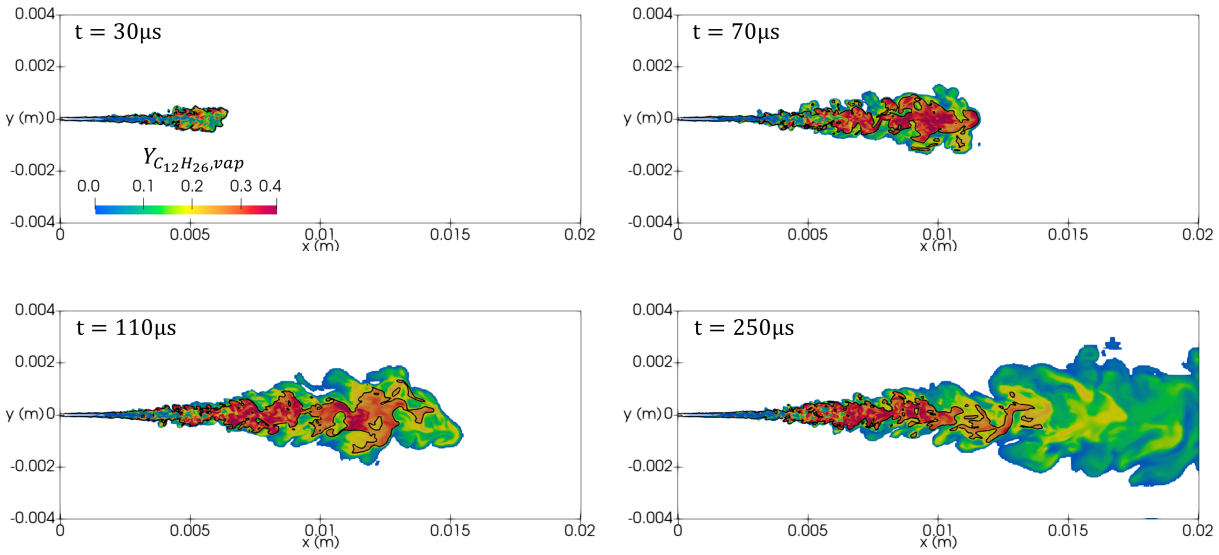

Figure 5.8: Evaporating Spray A condition: Temporal evolution of the vaporous n-dodecane mass fraction ($Y_{C_{12}H_{26},vap}$). Only cells with ($1e-03 < z_{N_2} < 0.999$) are shown. The black isoline represents reduced temperature ($T_r = 1$) to illustrate the subcritical and supercritical regions.

5.3 Effect of vaporization on the surface density and droplet size

In the current section, the effect of the vaporization on the surface area density and the SMD is investigated. The results are obtained under the evaporating condition with the same modeling constants ($C_\Sigma = 1, We_c = 1.5$) for the Σ equation used under the non-evaporating condition. The vaporization effect is analyzed in both the dense and diluted spray regions. The time averaged surface area density radial distribution at two axial positions in the dense ($x = 2\,\text{mm}$) and diluted ($x = 8\,\text{mm}$), spray regions under both the evaporating and non-evaporating conditions are depicted in Fig. 5.9. The time averaged results are indicated by the operator $\langle . \rangle$.

In the dense spray region ($x = 2\,\text{mm}$), it seems that the vaporization tends to enhance the surface generation, with relatively higher surface area density at the jet periphery than the non-evaporating case. The jet atomization can be mainly attributed to the growth of instabilities on the jet surface due to the turbulent interaction with the gas phase. However, under the evaporating condition, it is also affected by the ongoing evaporation, which tends to trigger and enhance the liquid jet instability. Indeed, the interaction between the counter flows of gas entrainment and evaporation at the interface can enhance its instability, as suggested in [79]. Besides, the variation of the properties would signifi-

cantly affect the surface density variation. For instance, the surface tension is reduced as the ambient pressure and temperature increase. Thus, higher surface generation could be expected under the evaporating condition compared to the non-evaporating condition.

On the other hand, at a relatively diluted spray region ($x = 8\,\text{mm}$), a reduction of the surface area density can be observed under the evaporating condition compared to the non-evaporating case. Meanwhile, as the liquid volume fraction decreases due to the ongoing evaporation, a relatively smaller mean SMD is obtained under the evaporating condition as shown in Fig. 5.10 at the same axial position ($x = 8\,\text{mm}$).

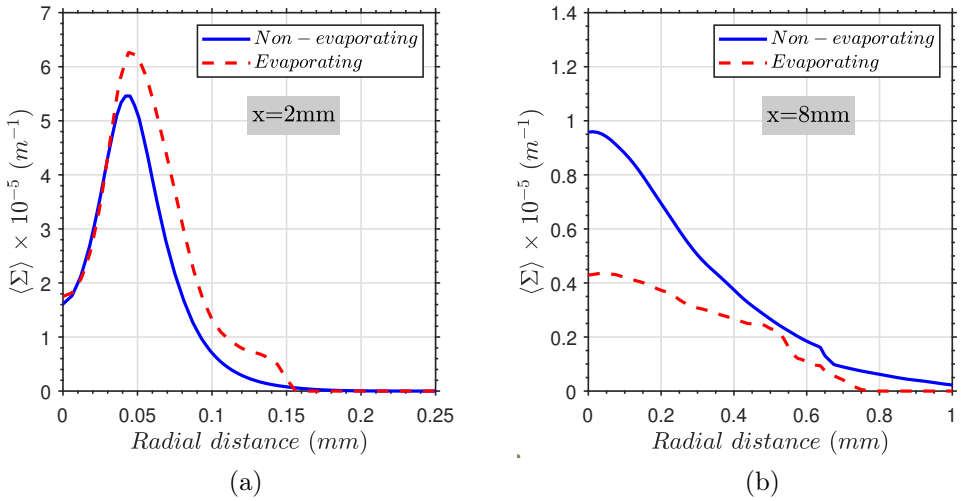

Figure 5.9: Time averaged surface area density radial distribution under non-evaporating and evaporating conditions at axial distances of (a) 2 mm and (b) 8 mm from the nozzle exit.

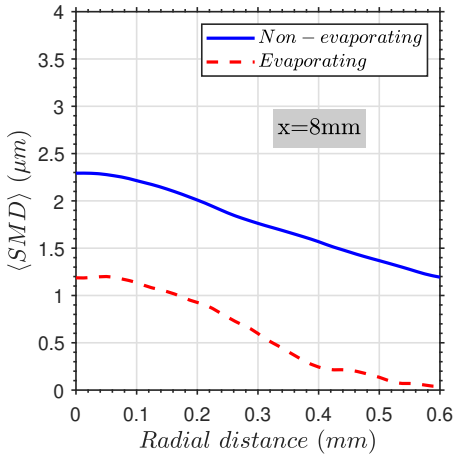

Figure 5.10: Time averaged SMD radial distribution under non-evaporating and evaporating conditions at axial distance of 8 mm from the nozzle exit.

These results confirm the sensitivity of the surface density model to the phase change. Indeed, in the current work, the phase change is implicitly considered through the terms (Σ_{min}) and (Σ_{eq}), which are dependent on (α_l) provided by the thermodynamic table.

Besides, the variation of the properties ($\rho_l, \rho_g, \sigma, ..., etc$) involved in the ($\Sigma$) equation with the temperature, pressure, and species mass fraction is considered by the thermodynamic table, which would also impact the predicted surface area density. Overall, the current model allows considering the phase change effect in both the dense and dilute zones of the spray without employing evaporation models assuming a spray of droplets as previously proposed in [45], for instance.

6 Conclusions

In this paper, a real fluid model (RFM) is proposed for the simulation of fuel injection and atomization under diesel-like operating conditions. The RFM is a fully compressible multi-component two-phase model closed by a thermodynamic equilibrium tabulation method based on a real-fluid EoS. The thermodynamic table considers both subcritical and supercritical thermodynamic states and allows an automatic transition between the different thermodynamic regimes. Besides, in the current study, the RFM model is supplemented with a surface density transport equation for atomization modeling within the LES framework. The proposed model is assessed using the non-evaporating and nominal (evaporating) conditions of the ECN Spray A injector.

Under the non-evaporating condition, the comparison of the LES-RFM results with the different experimental data in the near-nozzle field, including projected mass density, transverse integrated mass, and liquid volume fraction, has shown a good agreement, which indicates that the RFM model can accurately capture the fuel dispersion under the considered conditions. In addition, the surface density model assessment is carried out by comparing the model results against the experimental projected surface area density along the spray centerline and the SMD radial profiles. The obtained results show that the RFM model coupled with the surface density equation can reproduce well the experimental projected surface density along the spray axis. Besides, further comparison with the SMD measurements has demonstrated that the model prediction for the SMD falls within the experimental data range. Overall, it can be concluded that the proposed RFM model coupled with the surface density model can accurately predict the fuel dispersion and primary atomization under the considered conditions.

On the other hand, under the evaporating condition, global spray metrics such as spray liquid and vapor penetrations are well captured by the RFM model compared to the experimental data. Moreover, local analysis shows that the mixture fraction radial distribution favorably agrees with the experimental data within its confidence level. Further analysis of the surface density and SMD results has demonstrated the sensitivity of the surface area density model to the vaporization effects. In the dense region of the spray, vaporization tends to enhance the surface area density production, whereas vaporization decreases the surface area density in the dilute spray region. Besides, the mean SMD relatively decreases in the dilute region under the evaporating condition.

In summary, the present work shows that the proposed RFM model coupled with the surface density equation for fuel atomization modeling can capture well the fuel dispersion and atomization in the near-nozzle field along with global spray metrics and fuel mixture fraction distribution in the spray far-field, without exhaustive calibration of model constants as in classical Lagrangian spray models.

Indeed, the proposed model serves as a generalized approach that can represent a smooth transition from the subcritical to the supercritical regime as both can coexist under high-pressure/temperature conditions. In the context of fuel injection, the assump-

tions underlying the proposed model are particularly valid under high pressure injection conditions with dense sprays, where the droplet sizes are small. However, in case of a diluted spray with large droplets and significant slip velocity between the droplets and the gas phase, the employed homogeneous mixture approach with a single velocity for both phases will lose its validity. Accordingly, switching to a Lagrangian description of the spray could overcome such limitation. Future work also includes coupling of the external spray with the internal injector flow, and investigation of in-nozzle cavitation and turbulence development effects on the fuel dispersion and atomization.

Acknowledgments

This project has received funding from the European Union Horizon 2020 Research and Innovation programme. Grant Agreement no. 861002 for the EDEM project.

A Appendix

A.1 Validation of the Vapor-liquid equilibrium (VLE) computation

The vapor-liquid equilibrium calculation based on IFPEN-Carnot thermodynamic library using the VTPR-EOS employed in the current study is validated by computing the VLE of a binary mixture of (n-dodecane/nitrogen) and compared with the experimental data [28]. The binary interaction parameter ($k_{ij} = 0.19$) is employed in the current study. The critical parameters of each pure compound are summarized in Table. A.1. The comparison of the calculation results with the experimental data for the different isotherms is depicted in Fig. A.1, showing a satisfactory agreement for the majority of the considered pressures. The performed VLE calculations demonstrate the reliability of the IFPEN-Carnot thermodynamic library along with the VTPR-EoS to accurately model the considered binary mixture. It is also worth noting that the VLE calculation based on the PR-EoS would provide similar results to that using the VTPR-EoS, as volume translation does not influence the predicted phase equilibrium conditions. However, volume translation is employed to improve the liquid density prediction of the PR-EoS.

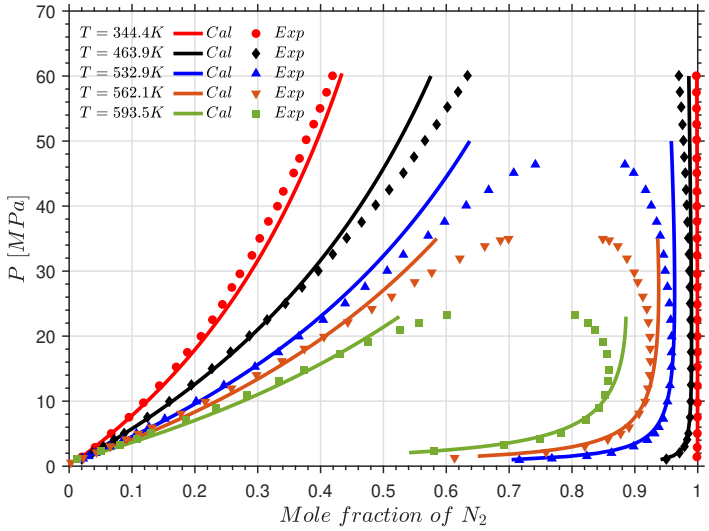

Figure A.1: Phase diagram of n-dodecane ($C_{12}H_{26}$) and nitrogen (N_2) binary mixture using the VTPR EoS.

Species	T_c (K)	P_c (bar)	ω
n-dodecane	658.1	18.2	0.57344
nitrogen	126.2	33.9	0.0403

Table A.1: Critical parameters of n-dodecane and nitrogen including, the critical temperature (T_c), critical pressure (P_c), and the acentric factor (ω).

A.2 Thermodynamic and transport properties

The calculation of the thermodynamic properties is performed based on the residual approach [18]. In this approach, any thermodynamic function (X) is computed from the sum of an ideal gas part (X^o) and a residual part (X^{res}). The ideal gas part is determined from a specific polynomial equation [57]. While the residual part, which represents the deviation from the ideal gas behavior, is deduced from the employed Equation of state (EoS). Regarding the evaluation of the transport properties, the thermal conductivity (λ) and dynamic viscosity (μ) are computed by the Chung et al. [15] correlations. The surface tension coefficient (σ) is computed by the Macleod-Sugden correlation [63] for the considered binary system of (n-dodecane/nitrogen).

The calculated properties of pure components (n-dodecane and nitrogen) using the PR and VTPR-EoS are compared with the NIST database [26] as depicted in Figs. (A.2, A.3). For the n-dodecane properties, the predicted density by the VTPR-EoS favorably agrees with the NIST reference data, especially for the low-temperature range, where the original PR EoS underestimates the fuel density. Besides, the predicted isobaric heat capacity and sound speed by the VTPR and PR EoSs show good agreement with the reference data. However, in the low-temperature range, the overestimation of the sound speed is slightly higher by the VTPR-EoS compared to the PR-EoS.

For the nitrogen properties, Fig. A.3 shows that the VTPR-EoS results match with great accuracy the NIST reference data. It is worth noting that for nitrogen properties, both the VTPR and PR EoSs provide the same results.

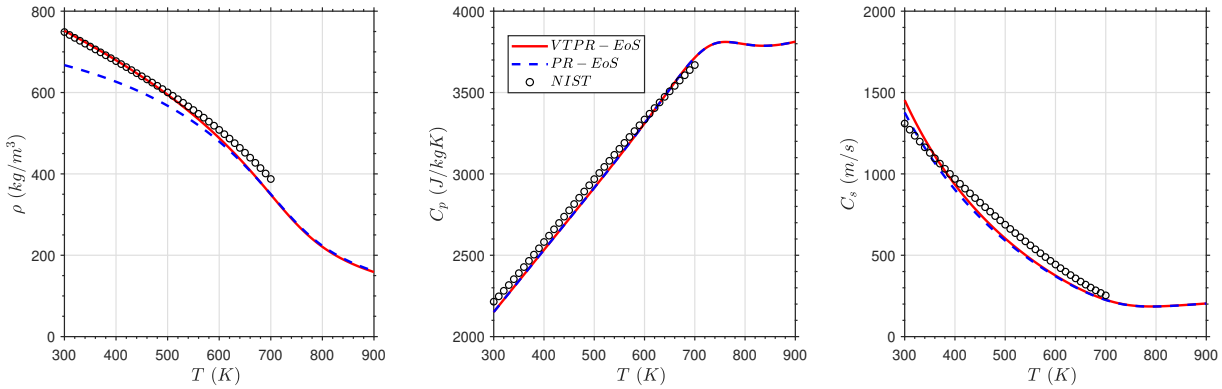

(a) (b) (c)

Figure A.2: Comparison of the PR and VTPR EoSs prediction for the (a) density, (b) isobaric heat capacity, and (c) sound speed of pure n-dodecane against NIST [26] reference data at $P = 6\,\mathrm{MPa}$.

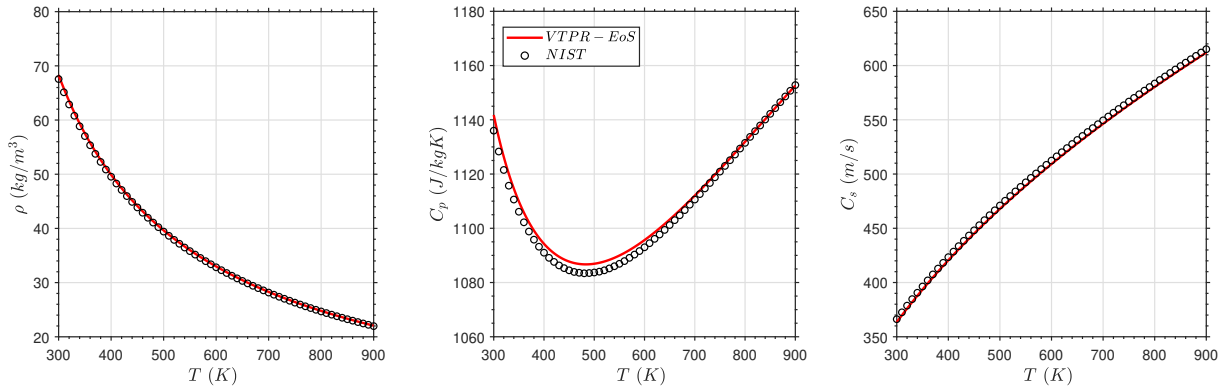

(a) (b) (c)

Figure A.3: Comparison of the VTPR EoS prediction for the (a) density, (b) isobaric heat capacity, and (c) sound speed of pure nitrogen against NIST [26] reference data at $P = 6\,\mathrm{MPa}$.

Furthermore, the computation of the two-phase mixture properties is obtained from the liquid and gas phase properties as described through Equations (A.1-A.7)

$$\rho = \sum_p \alpha_p \rho_p \tag{A.1}$$

$$e = \frac{1}{\rho} \sum_p \alpha_p \rho_p e_p \tag{A.2}$$

$$\lambda = \frac{1}{\rho} \sum_p \alpha_p \rho_p \lambda_p \tag{A.3}$$

$$\mu = \sum_p \alpha_p \mu_p \tag{A.4}$$

$$C_p = \frac{1}{\rho} \sum_p \alpha_p \rho_p C_{p_p} \tag{A.5}$$

$$C_v = \frac{1}{\rho} \sum_p \alpha_p \rho_p C_{v_p} \tag{A.6}$$

$$\frac{1}{\rho C^2_{s,mix,Wood}} = \sum_p \frac{\alpha_p}{\rho_p C^2_{s,p}} \tag{A.7}$$

where, (α_p) is the phase volume fraction and $(p = l, v)$ stands for liquid and vapor phases, respectively. $(\rho, e, \lambda, \mu, C_p, C_v, C_{s,mix,Wood})$ are the two-phase mixture density, specific internal energy, thermal conductivity, dynamic viscosity, specific heats at constant pressure and volume and Wood speed of sound [75].

The variation of the mixture properties for the binary mixture of (n- dodecane/nitrogen) at ($P = 6\,\text{MPa}$) is shown in Fig. A.4. These results show the variation of the different properties as a function of the temperature and species mass fraction. Besides, it demonstrates that the employed real-fluid EoS can capture the non-linearity of the properties at the considered transcritical regime.

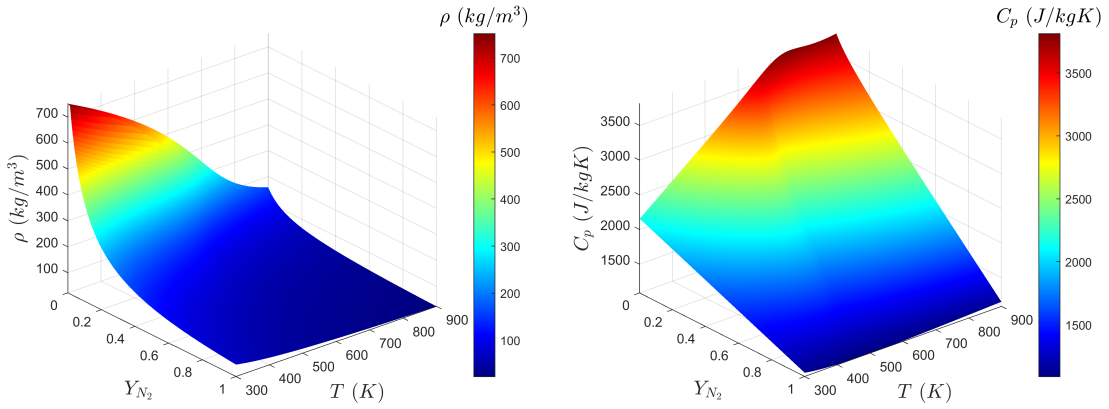

(a) (b)

Figure A.4: Contour plots of (a) mixture density and (b) mixture heat capacity for n-dodecane ($C_{12}H_{26}$) and nitrogen (N_2) binary mixture at $P = 6\,\text{MPa}$ using the VTPR EoS. (Color online)

A.3 Solution procedure of the Real-fluid model

The solution procedure of the proposed real-fluid model using a modified PISO algorithm [35] in CONVERGE CFD solver is summarized in the current section. The solution procedure flow chart is shown in Fig. A.5 and can be summarized as follows:

- Solve the momentum predictor followed by the first corrector step, which includes solving the pressure equation then updating the velocity.
- Solve the transport equations in the order shown in the PISO loop in the flow chart.
- After PISO convergence, the surface area density equation is solved, followed by evaluating the turbulence quantities.

Here in the flow chart, (*Reverse look-up*) indicates the evaluation of the temperature from (e, P, Y_k), while (*Table look-up*) indicates the evaluation of any property from the (T, P, Y_k) as previously explained in section 2.2. More detailed description of the coupling of the flow solver with the thermodynamic table can also be found in the authors previous work [35].

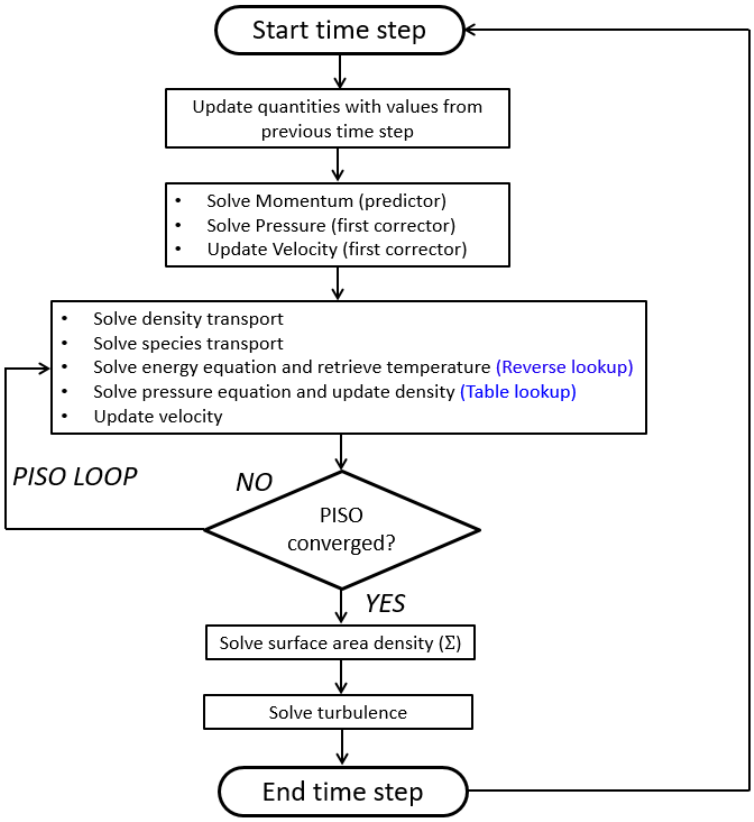

Figure A.5: Flow chart of the solution procedure of the real-fluid model governing equations using the PISO algorithm

References

[1] Engine Combustion Network (ECN), Spray A geometry. URL `https://ecn.sandia.gov/diesel-spray-combustion/target-condition/spray-a-nozzle-geometry`.

[2] Engine Combustion Network (ECN), Near-nozzle mixture derived from x-ray radiography. URL `https://ecn.sandia.gov/rad675/`.

[3] Engine Combustion Network (ECN), Modeling Standards and Recommendations. URL `https://ecn.sandia.gov/diesel-spray-combustion/computational-method/modeling-standards/`.

[4] Engine Combustion Network (ECN), Measurements of the liquid length for nozzle 210675 using diffused back-illumination (DBI) at Spray A and other conditions. URL `https://ecn.sandia.gov/data/dbi675/`.

[5] CMT, Virtual Injection Rate Generator. URL https://www.cmt.upv.es/ECN03.aspx.

[6] Engine Combustion Network (ECN), Rayleigh scattering n-dodecane/ambient mixing images for Spray A and several other experimental conditions. URL https://ecn.sandia.gov/data/bkldaal4mixing/.

[7] Engine Combustion Network (ECN), Diesel Data Search, . URL https://ecn.sandia.gov/ecn-data-search.

[8] Engine Combustion Network (ECN), . URL https://ecn.sandia.gov.

[9] A. Ahmed, G. Tretola, S. Navarro-Martinez, K. Vogiatzaki, B. Duret, J. Reveillon, and F.-X. Demoulin. Atomization modeling using surface density and stochastic fields. *Atomization and Sprays*, 30(4):239–266, 2020. ISSN 1044-5110. doi: 10.1615/AtomizSpr.2020032620.

[10] J. Anez, A. Ahmed, N. Hecht, B. Duret, J. Reveillon, and F. X. Demoulin. Eulerian–Lagrangian spray atomization model coupled with interface capturing method for diesel injectors. *International Journal of Multiphase Flow*, 113:325–342, 2019. ISSN 03019322. doi: 10.1016/j.ijmultiphaseflow.2018.10.009.

[11] M. Bardi, R. Payri, L. M. Malbec, G. Bruneaux, L. M. Pickett, J. Manin, T. Bazyn, and C. Genzale. Engine Combustion Network: Comparison of spray development, vaporization, and combustion in different combustion vessels. *Atomization and Sprays*, 22(10):807–842, 2012. ISSN 1044-5110. doi: 10.1615/AtomizSpr.2013005837.

[12] M. Battistoni, G. M. Magnotti, C. L. Genzale, M. Arienti, K. E. Matusik, D. J. Duke, J. Giraldo, J. Ilavsky, A. L. Kastengren, C. F. Powell, and P. Marti-Aldaravi. Experimental and Computational Investigation of Subcritical Near-Nozzle Spray Structure and Primary Atomization in the Engine Combustion Network Spray D. *SAE International Journal of Fuels and Lubricants*, 11(4):337–352, 2018. ISSN 1946-3960. doi: 10.4271/2018-01-0277.

[13] G. Blokkeel, B. Barbeau, and R. Borghi. A 3D Eulerian Model to Improve the Primary Breakup of Atomizing Jet. In *SAE Technical Paper Series*, SAE Technical Paper Series. SAE International400 Commonwealth Drive, Warrendale, PA, United States, 2003. doi: 10.4271/2003-01-0005.

[14] J. Chesnel, J. Reveillon, T. Menard, and F.-X. Demoulin. Large eddy simulation of liquid jet atomization. *Atomization and Sprays*, 21(9):711–736, 2011. ISSN 1044-5110. doi: 10.1615/AtomizSpr.2012003740.

[15] T. H. Chung, M. Ajlan, L. L. Lee, and K. E. Starling. Generalized multiparameter correlation for nonpolar and polar fluid transport properties. *Industrial & Engineering Chemistry Research*, 27(4):671–679, 1988. ISSN 0888-5885. doi: 10.1021/ie00076a024.

[16] C. Crua, J. Manin, and L. M. Pickett. On the transcritical mixing of fuels at diesel engine conditions. *Fuel*, 208:535–548, 2017. ISSN 0016-2361. doi: 10.1016/j.fuel.2017.06.091.

[17] L. Davidson and M. Billson. Hybrid LES-RANS using synthesized turbulent fluctuations for forcing in the interface region. *International Journal of Heat and Fluid Flow*, 27(6):1028–1042, 2006. doi: 10.1016/j.ijheatfluidflow.2006.02.025.

[18] J.-C. de Hemptinne, J.-M. Ledanois, P. Mougin, and A. Barreau. *Select Thermodynamic Models for Process Simulation - A Practical Guide using a Three Steps Methodology*. Technip, 2012. ISBN 9782901638131. doi: 10.2516/ifpen/2011001.

[19] F.-X. Demoulin, J. Reveillon, B. Duret, Z. Bouali, P. Desjonqueres, and T. Menard. Toward using direct numerical simulation to improve primary break-up modeling. *Atomization and Sprays*, 23(11):957–980, 2013. ISSN 1044-5110. doi: 10.1615/AtomizSpr.2013007439.

[20] J. M. Desantes, J. M. Garcia-Oliver, J. M. Pastor, and A. Pandal. A comparison of diesel sprays CFD modeling approaches: DDM versus Σ-Y Eulerian atomization model. *Atomization and Sprays*, 26(7):713–737, 2016. ISSN 1044-5110. doi: 10.1615/AtomizSpr.2015013285.

[21] J. M. Desantes, J. M. García-Oliver, J. M. Pastor, A. Pandal, E. Baldwin, and D. P. Schmidt. Coupled/decoupled spray simulation comparison of the ECN spray a condition with the -Y Eulerian atomization model. *International Journal of Multiphase Flow*, 80:89–99, 2016. ISSN 03019322. doi: 10.1016/j.ijmultiphaseflow.2015.12.002.

[22] J. M. Desantes, J. M. García-Oliver, J. M. Pastor, I. Olmeda, A. Pandal, and B. Naud. LES Eulerian diffuse-interface modeling of fuel dense sprays near- and far-field. *International Journal of Multiphase Flow*, 127:103272, 2020. ISSN 03019322. doi: 10.1016/j.ijmultiphaseflow.2020.103272.

[23] B. M. Devassy, C. Habchi, and E. Daniel. Atomization modelling of liquid jets using a two-surface-density approach. *Atomization and Sprays*, 25(1):47–80, 2015. ISSN 1044-5110. doi: 10.1615/AtomizSpr.2014011350.

[24] J. K. Dukowicz. A particle-fluid numerical model for liquid sprays. *Journal of Computational Physics*, 35(2):229–253, 1980. ISSN 00219991. doi: 10.1016/0021-9991(80)90087-X.

[25] B. Duret, J. Reveillon, T. Menard, and F. X. Demoulin. Improving primary atomization modeling through DNS of two-phase flows. *International Journal of Multiphase Flow*, 55:130–137, 2013. ISSN 03019322. doi: 10.1016/j.ijmultiphaseflow.2013.05.004.

[26] E.W. Lemmon, M.L. Huber, M.O. McLinden. NIST reference fluid thermodynamic and transport properties–REFPROP. 2002.

[27] H. Gaballa, S. Jafari, C. Habchi, and J.-C. de Hemptinne. Numerical investigation of droplet evaporation in high-pressure dual-fuel conditions using a tabulated real-fluid model. *International Journal of Heat and Mass Transfer*, 189:122671, 2022. ISSN 00179310. doi: 10.1016/j.ijheatmasstransfer.2022.122671.

[28] T. García-Córdova, D. N. Justo-García, B. E. García-Flores, and F. García-Sánchez. Vapor−Liquid Equilibrium Data for the Nitrogen + Dodecane System at Temperatures from (344 to 593) K and at Pressures up to 60 MPa. *Journal of Chemical & Engineering Data*, 56(4):1555–1564, 2011. ISSN 0021-9568. doi: 10.1021/je1012372.

[29] J. M. Garcia-Oliver, J. M. Pastor, A. Pandal, N. Trask, E. Baldwin, and D. P. Schmidt. DIESEL SPRAY CFD SIMULATIONS BASED ON THE S-ÎŸ EULERIAN ATOMIZATION MODEL. *Atomization and Sprays*, 23(1):71–95, 2013. ISSN 1044-5110. doi: 10.1615/AtomizSpr.2013007198.

[30] C. Habchi. The Energy Spectrum Analogy Beakup (SAB) Model for the Numerical Simulation of Sprays. *Atomization and Sprays*, 21(12):1033–1057, 2011. ISSN 1044-5110. doi: 10.1615/AtomizSpr.2012004531.

[31] C. Habchi and G. Bruneaux. LES and Experimental investigation of Diesel sprays. *12th ICLASS Triennial Int. Conf. on Liquid Atomization and Spray Systems,Heidelberg, Germany*, 2012. doi: 10.13140/2.1.1044.0648.

[32] M. Herrmann. On simulating primary atomization using the refined level set grid method. *Atomization and Sprays*, 21(4):283–301, 2011. ISSN 1044-5110. doi: 10.1615/AtomizSpr.2011002760.

[33] C. Hirt and B. Nichols. Volume of fluid (VOF) method for the dynamics of free boundaries. *Journal of Computational Physics*, 39(1):201–225, 1981. ISSN 00219991. doi: 10.1016/0021-9991(81)90145-5.

[34] R. Issa. Solution of the implicitly discretised fluid flow equations by operator-splitting. *Journal of Computational Physics*, 62(1):40–65, 1986. ISSN 00219991. doi: 10.1016/0021-9991(86)90099-9.

[35] S. Jafari, H. Gaballa, C. Habchi, and J.-C. de Hemptinne. Towards Understanding the Structure of Subcritical and Transcritical Liquid–Gas Interfaces Using a Tabulated Real Fluid Modeling Approach. *Energies*, 14(18):5621, 2021. ISSN 1996-1073. doi: 10.3390/en14185621.

[36] S. Jafari, H. Gaballa, C. Habchi, J.-C. de Hemptinne, and P. Mougin. Exploring the interaction between phase separation and turbulent fluid dynamics in multi-species supercritical jets using a tabulated real-fluid model. *The Journal of Supercritical Fluids*, page 105557, 2022. ISSN 08968446. doi: 10.1016/j.supflu.2022.105557.

[37] M. Jia, H. Pan, Y. Bian, Z. Zhang, Y. Chang, and H. Liu. Calibration of the constants in the Kelviv-Helmholtz Rayleigh-Taylor (KH-RT) breakup model for diesel spray under wide conditions based on advanced data analysis techniques. *Atomization and Sprays*, 32(6):1–27, 2022. ISSN 1044-5110. doi: 10.1615/AtomizSpr.2022040203.

[38] A. Kastengren, J. Ilavsky, J. P. Viera, R. Payri, D. J. Duke, A. Swantek, F. Z. Tilocco, N. Sovis, and C. F. Powell. Measurements of droplet size in shear-driven atomization using ultra-small angle x-ray scattering. *International Journal of Multiphase Flow*, 92:131–139, 2017. ISSN 03019322. doi: 10.1016/j.ijmultiphaseflow.2017.03.005.

[39] A. L. Kastengren, C. F. Powell, Y. Wang, K.-S. Im, and J. Wang. X-ray radiography measurements of diesel spray structure at engine-like ambient density. *Atomization and Sprays*, 19(11):1031–1044, 2009. ISSN 1044-5110. doi: 10.1615/AtomizSpr.v19.i11.30.

[40] A. L. Kastengren, F. Tilocco, D. Duke, and C. F. Powel. Time-Resolved X-Ray Radiography of Diesel Injectors from the Engine Combustion Network. *ICLASS 2012, 12th Triennial International Conference on Liquid Atomization and Spray Systems*, 2012.

[41] P. Koukouvinis, A. Vidal-Roncero, C. Rodriguez, M. Gavaises, and L. Pickett. High pressure/high temperature multiphase simulations of dodecane injection to nitrogen: Application on ECN Spray-A. *Fuel*, 275:117871, 2020. ISSN 0016-2361. doi: 10.1016/j.fuel.2020.117871.

[42] P. Koukouvinis, C. Rodriguez, J. Hwang, I. Karathanassis, M. Gavaises, and L. Pickett. Machine Learning and transcritical sprays: A demonstration study of their potential in ECN Spray-A. *International Journal of Engine Research*, page 146808742110202, 2021. ISSN 1468-0874. doi: 10.1177/14680874211020292.

[43] G. Lacaze, A. Misdariis, A. Ruiz, and J. C. Oefelein. Analysis of high-pressure Diesel fuel injection processes using LES with real-fluid thermodynamics and transport. *Proceedings of the Combustion Institute*, 35(2):1603–1611, 2015. ISSN 15407489. doi: 10.1016/j.proci.2014.06.072.

[44] R. Lebas, G. Blokkeel, P.-A. Beau, and F.-X. Demoulin. Coupling Vaporization Model With the Eulerian-Lagrangian Spray Atomization (ELSA) Model in Diesel Engine Conditions. In *SAE Technical Paper Series*, SAE Technical Paper Series. SAE International400 Commonwealth Drive, Warrendale, PA, United States, 2005. doi: 10.4271/2005-01-0213.

[45] R. Lebas, T. Menard, P. A. Beau, A. Berlemont, and F. X. Demoulin. Numerical simulation of primary break-up and atomization: DNS and modelling study. *International Journal of Multiphase Flow*, 35(3):247–260, 2009. ISSN 03019322. doi: 10.1016/j.ijmultiphaseflow.2008.11.005.

[46] G. M. Magnotti and C. L. Genzale. Detailed assessment of diesel spray atomization models using visible and X-ray extinction measurements. *International Journal of Multiphase Flow*, 97:33–45, 2017. ISSN 03019322. doi: 10.1016/j.ijmultiphaseflow.2017.08.002.

[47] J. Manin, M. Bardi, and L. M. Pickett. Evaluation of the liquid length via diffused back-illumination imaging in vaporizing diesel sprays. *The Eighth International Conference on Modeling and Diagnostics for Advanced Engine Systems (COMODIA)*, pages 665–673, 2012.

[48] J. Manin, M. Bardi, L. M. Pickett, R. N. Dahms, and J. C. Oefelein. Microscopic investigation of the atomization and mixing processes of diesel sprays injected into high pressure and temperature environments. *Fuel*, 134:531–543, 2014. ISSN 0016-2361. doi: 10.1016/j.fuel.2014.05.060.

[49] J. Matheis and S. Hickel. Multi-component vapor-liquid equilibrium model for LES of high-pressure fuel injection and application to ECN Spray A. *International Journal of Multiphase Flow*, 99:294–311, 2018. ISSN 03019322. doi: 10.1016/j.ijmultiphaseflow.2017.11.001.

[50] T. Ménard, S. Tanguy, and A. Berlemont. Coupling level set/VOF/ghost fluid methods: Validation and application to 3D simulation of the primary break-up of a liquid jet. *International Journal of Multiphase Flow*, 33(5):510–524, 2007. ISSN 03019322. doi: 10.1016/j.ijmultiphaseflow.2006.11.001.

[51] M. L. Michelsen. The isothermal flash problem. Part II. Phase-split calculation. *Fluid Phase Equilibria*, 9(1):21–40, 1982. ISSN 03783812. doi: 10.1016/0378-3812(82)85002-4.

[52] F. Nicoud, H. B. Toda, O. Cabrit, S. Bose, and J. Lee. Using singular values to build a subgrid-scale model for large eddy simulations. *Physics of Fluids*, 23(8):085106, 2011. ISSN 1070-6631. doi: 10.1063/1.3623274.

[53] P. Pakseresht and S. V. Apte. Volumetric displacement effects in Euler-Lagrange LES of particle-laden jet flows. *International Journal of Multiphase Flow*, 113:16–32, 2019. ISSN 03019322. doi: 10.1016/j.ijmultiphaseflow.2018.12.013.

[54] A. Panchal and S. Menon. A hybrid Eulerian-Eulerian/Eulerian-Lagrangian method for dense-to-dilute dispersed phase flows. *Journal of Computational Physics*, 439:110339, 2021. ISSN 00219991. doi: 10.1016/j.jcp.2021.110339.

[55] A. Pandal, J. M. Pastor, R. Payri, A. Kastengren, D. Duke, K. Matusik, J. S. Giraldo, C. Powell, and D. Schmidt. Computational and Experimental Investigation of Interfacial Area in Near-Field Diesel Spray Simulation. *SAE International Journal of Fuels and Lubricants*, 10(2):423–431, 2017. ISSN 1946-3960. doi: 10.4271/2017-01-0859.

[56] A. Pandal, B. M. Ningegowda, F. Rahantamialisoa, J. Zembi, H. G. Im, and M. Battistoni. Development of a drift-flux velocity closure for a coupled Σ -Y spray atomization model. *International Journal of Multiphase Flow*, 141:103691, 2021. ISSN 03019322. doi: 10.1016/j.ijmultiphaseflow.2021.103691.

[57] C. A. Passut and R. P. Danner. Correlation of Ideal Gas Enthalpy, Heat Capacity and Entropy. *Industrial & Engineering Chemistry Process Design and Development*, 11(4):543–546, 1972. ISSN 0196-4305. doi: 10.1021/i260044a016.

[58] D.-Y. Peng and D. B. Robinson. A New Two-Constant Equation of State. *Industrial & Engineering Chemistry Fundamentals*, 15(1):59–64, 1976. ISSN 0196-4313. doi: 10.1021/i160057a011.

[59] L. M. Pickett, J. Manin, C. L. Genzale, D. L. Siebers, M. P. B. Musculus, and C. A. Idicheria. Relationship Between Diesel Fuel Spray Vapor Penetration/Dispersion and Local Fuel Mixture Fraction. *SAE International Journal of Engines*, 4(1):764–799, 2011. ISSN 1946-3944. doi: 10.4271/2011-01-0686.

[60] L. M. Pickett, J. Manin, A. Kastengren, and C. Powell. Comparison of Near-Field Structure and Growth of a Diesel Spray Using Light-Based Optical Microscopy and X-Ray Radiography. *SAE International Journal of Engines*, 7(2):1044–1053, 2014. ISSN 1946-3944. doi: 10.4271/2014-01-1412.

[61] L. M. Pickett, C. L. Genzale, and J. Manin. Uncertainty quantification for liquid penetration of evaporating sprays at diesel-like conditions. *Atomization and Sprays*, 25(5):425–452, 2015. ISSN 1044-5110. doi: 10.1615/AtomizSpr.2015010618.

[62] J. Poblador-Ibanez and W. A. Sirignano. Temporal atomization of a transcritical liquid n-decane jet into oxygen. *International Journal of Multiphase Flow*, 153:104130, 2022. ISSN 03019322. doi: 10.1016/j.ijmultiphaseflow.2022.104130.

[63] B. E. Poling, J. M. Prausnitz, and J. P. O'Connell. *The properties of gases and liquids*. McGraw-Hill, New York and Bogota and Milan etc., 5th ed. edition, 2001. ISBN 9780070116825.

[64] S. B. Pope. Ten questions concerning the large-eddy simulation of turbulent flows. *New Journal of Physics*, 6:35, 2004. doi: 10.1088/1367-2630/6/1/035.

[65] R. D. Reitz. Modeling atomization processes in high-pressure vaporizing sprays. *Atomisation and Spray technology*, 3:309–337, 1987.

[66] Richards, K.J., Senecal, P.K., and Pomraning, E. CONVERGE 3.0, Convergent Science, Madison, WI (2021).

[67] J. Shinjo. Recent Advances in Computational Modeling of Primary Atomization of Liquid Fuel Sprays. *Energies*, 11(11):2971, 2018. ISSN 1996-1073. doi: 10.3390/en11112971.

[68] J. Shinjo and A. Umemura. Simulation of liquid jet primary breakup: Dynamics of ligament and droplet formation. *International Journal of Multiphase Flow*, 36(7): 513–532, 2010. ISSN 03019322. doi: 10.1016/j.ijmultiphaseflow.2010.03.008.

[69] M. Sussman, P. Smereka, and S. Osher. A Level Set Approach for Computing Solutions to Incompressible Two-Phase Flow. *Journal of Computational Physics*, 114(1): 146–159, 1994. ISSN 00219991. doi: 10.1006/jcph.1994.1155.

[70] G. Tretola, K. Vogiatzaki, and S. Navarro-Martinez. Implementation of a probabilistic surface density volume of fluid approach for spray atomisation. *Computers & Fluids*, 230:105121, 2021. ISSN 00457930. doi: 10.1016/j.compfluid.2021.105121.

[71] U. Unnikrishnan, J. C. Oefelein, and V. Yang. Subgrid modeling of the filtered equation of state with application to real-fluid turbulent mixing at supercritical pressures. *Physics of Fluids*, 34(6):065112, 2022. ISSN 1070-6631. doi: 10.1063/5.0088074.

[72] A. Vallet and R. Borghi. Modélisation eulerienne de l'atomisation d'un jet liquide. *Comptes Rendus de l'Académie des Sciences - Series IIB - Mechanics-Physics-Astronomy*, 327(10):1015–1020, 1999. ISSN 12874620. doi: 10.1016/S1287-4620(00)87013-1.

[73] A. Vallet, A. A. Burluka, and R. Borghi. Development of a eulerian model for the "atomization" of a liquid jet. *Atomization and Sprays*, 11(6):24, 2001. ISSN 1044-5110. doi: 10.1615/AtomizSpr.v11.i6.20.

[74] C. Ware, W. Knight, and D. Wells. Memory intensive statistical algorithms for multibeam bathymetric data. *Computers & Geosciences*, 17(7):985–993, 1991. ISSN 00983004. doi: 10.1016/0098-3004(91)90093-S.

[75] A. B. Wood and R. B. Lindsay. A Textbook of Sound. *Physics Today*, 9(11):37, 1956. ISSN 0031-9228. doi: 10.1063/1.3059819.

[76] Q. Xue, S. Som, P. K. Senecal, and E. Pomraning. Large Eddy Simulation of fuel-spray under non-reacting IC engine conditions. *Atomization and Sprays*, 23(10): 925–955, 2013. ISSN 1044-5110. doi: 10.1615/AtomizSpr.2013008320.

[77] Q. Xue, M. Battistoni, C. F. Powell, D. E. Longman, S. P. Quan, E. Pomraning, P. K. Senecal, D. P. Schmidt, and S. Som. An Eulerian CFD model and X-ray radiography for coupled nozzle flow and spray in internal combustion engines. *International Journal of Multiphase Flow*, 70:77–88, 2015. ISSN 03019322. doi: 10.1016/j.ijmultiphaseflow.2014.11.012.

[78] B. Yang, Q. Duan, B. Liu, and K. Zeng. Parametric investigation of low pressure dual-fuel direct injection on the combustion performance and emissions characteristics in a RCCI engine fueled with diesel and CH4. *Fuel*, 260:116408, 2020. ISSN 0016-2361. doi: 10.1016/j.fuel.2019.116408.

[79] S. Yang, P. Yi, and C. Habchi. Real-fluid injection modeling and LES simulation of the ECN Spray A injector using a fully compressible two-phase flow approach. *International Journal of Multiphase Flow*, 122:103145, 2020. ISSN 03019322. doi: 10.1016/j.ijmultiphaseflow.2019.103145.

[80] P. Yi, S. Yang, C. Habchi, and R. Lugo. A multicomponent real-fluid fully compressible four-equation model for two-phase flow with phase change. *Physics of Fluids*, 31 (2):026102, 2019. ISSN 1070-6631. doi: 10.1063/1.5065781.

[81] Z. Yue and R. D. Reitz. An equilibrium phase spray model for high-pressure fuel injection and engine combustion simulations. *International Journal of Engine Research*, 20(2):203–215, 2019. ISSN 1468-0874. doi: 10.1177/1468087417744144.

[82] H. Zhang and S. Yang. Multi-component transcritical flow simulation using in situ adaptive tabulation of vapor-liquid equilibrium solutions. *in ILASS-Americas 31st Annual Conference on Liquid Atomization and Spray Systems*, 2021.